

General relativistic hydrodynamics with viscosity: contraction, catastrophic collapse, and disk formation in hypermassive neutron stars

Matthew D. Duez, Yuk Tung Liu, Stuart L. Shapiro,* and Branson C. Stephens
Department of Physics, University of Illinois at Urbana-Champaign, Urbana, IL 61801

Viscosity and magnetic fields drive differentially rotating stars toward uniform rotation, and this process has important consequences in many astrophysical contexts. For example, merging binary neutron stars can form a “hypermassive” remnant, i.e. a differentially rotating star with a mass greater than would be possible for a uniformly rotating star. The removal of the centrifugal support provided by differential rotation can lead to delayed collapse of the remnant to a black hole, accompanied by a delayed burst of gravitational radiation. Both magnetic fields and viscosity alter the structure of differentially rotating stars on secular timescales, and tracking this evolution presents a strenuous challenge to numerical hydrodynamic codes. Here, we present the first evolutions of rapidly rotating stars with shear viscosity in full general relativity. We self-consistently include viscosity in our relativistic hydrodynamic code by solving the fully relativistic Navier-Stokes equations. We perform these calculations both in axisymmetry and in full 3+1 dimensions. In axisymmetry, the resulting reduction in computational costs allows us to follow secular evolution with high resolution over dozens of rotation periods (thousands of M). We find that viscosity operating in a hypermassive star generically leads to the formation of a compact, uniformly rotating core surrounded by a low-density disk. These uniformly rotating cores are often unstable to gravitational collapse. We follow the collapse in such cases and determine the mass and the spin of the final black hole and ambient disk. However, viscous braking of differential rotation in hypermassive neutron stars does not always lead to catastrophic collapse, especially when viscous heating is substantial. The stabilizing influences of viscous heating, which generates enhanced thermal pressure, and centrifugal support prevent collapse in some cases, at least until the star cools. In all cases studied, the rest mass of the resulting disk is found to be 10-20% of the original star, whether surrounding a uniformly rotating core or a rotating black hole. This study represents an important step toward understanding secular effects in relativistic stars and foreshadows more detailed, future simulations, including those involving magnetic fields.

PACS numbers: 04.25.Dm, 04.40.Dg, 97.60.Jd

I. INTRODUCTION

The field of numerical relativity has matured to a stage where it is possible to simulate realistic systems of astrophysical interest. In this paper, we examine the global effects of viscosity on differentially rotating, relativistic stars. Viscosity can have significant effects on the stability of neutron stars. For example, it can drive a secular bar instability in rapidly rotating neutron stars, as shown in Newtonian gravitation [1, 2] and in general relativity [3]. Viscosity can suppress the r -modes [4, 5] and other gravitational-radiation driven instabilities, including the secular bar modes [6]. Viscosity also destroys differential rotation, and this can cause significant changes in the structure and evolution of differentially rotating massive neutron stars.

Differentially rotating neutron stars can support significantly more rest mass than their nonrotating or uniformly rotating counterparts, making “hypermassive” neutron stars possible [7, 8]. Such hypermassive neutron stars can form from the coalescence of neutron star binaries [9, 10, 11] or from rotating core collapse. The

stabilization arising from differential rotation, although expected to last for many dynamical timescales, will ultimately be destroyed by magnetic braking and/or viscosity [7, 12]. These processes drive the star to uniform rotation, which cannot support the full mass of the hypermassive remnant. This process can lead to “delayed” catastrophic collapse to a black hole, possibly accompanied by some mass loss. Such a delayed collapse might emit a delayed gravitational wave signal detectable by laser interferometers. Moreover, the collapse, together with any residual gas in an ambient accretion disk, could be the origin of a gamma-ray burst (GRB).

Both magnetic fields and viscosity can destroy differential rotation in a rapidly rotating star [12, 13, 14]. Simple estimates show that the magnetic braking (Alfvén) timescale for a laminar field is much shorter than the timescale of molecular (neutron) viscosity in a typical massive neutron star. Hence magnetic fields are expected to be the principal mechanism driving neutron stars toward rigid rotation. Phase mixing arising from magnetic braking [14, 15], or other possible magnetohydrodynamic instabilities [15, 16] might stir up turbulence. Turbulent shear viscosity could then dominate the subsequent evolution. In this paper, we are primarily interested in identifying the global evolutionary consequences of shear viscosity in a relativistic star, independent of the detailed nature or origin of the viscosity.

*Department of Astronomy & NCSA, University of Illinois at Urbana-Champaign, Urbana, IL 61801

To explore the consequences of the loss of differential rotation in equilibrium stars, we study the secular evolution of differentially rotating relativistic stars in the presence of a shear viscosity. Viscosity and magnetic fields have two things in common: (1) they both change the angular velocity profiles of a differentially rotating star, and (2) they both act on *secular* timescales, which can be many rotation periods. The latter inequality poses a severe challenge to numerical simulations using a hydrodynamic code. It is too taxing for a *hydrodynamic* code using an explicit differencing scheme to evolve a star for physical realistic secular timescales. To solve this problem, we artificially amplify the strength of viscosity so that the viscous timescale is short enough for numerical treatment. However, we keep the viscous timescale substantially longer than the dynamical timescale of the stars, so that the evolution of the star remains quasi-stationary. We then check the validity of our results by reducing the viscosity on successive runs and testing that the viscosity-induced physical behavior is unchanged; rather, only the timescale changes and does so inversely with the strength of viscosity. A more detailed discussion of the expected scaling is presented in Section IIE [17].

To study viscous evolution, we need to perform long simulations in full general relativity. Typically, we evolve the stars in axisymmetry. This allows us to follow the secular evolution of the stars with high resolution in a reasonable amount of time. Viscosity can, however, drive nonaxisymmetric instabilities when a star is rapidly rotating. To test for such instabilities, we also perform lower-resolution, three-dimensional (3D) simulations on the most rapidly rotating stars we consider.

For non-hypermassive neutron stars that are slowly and differentially rotating, we find that viscosity simply drives the whole star to rigid rotation. If the non-hypermassive neutron star is rapidly and differentially rotating, however, viscosity drives the inner core to rigid rotation and, at the same time, expels the material in the outer layers. The final system in this case consists of a rigidly-rotating core surrounded by a low-density, ambient disk in quasi-stationary equilibrium.

Our most interesting results concern the fate of hypermassive neutron stars. We numerically evolve four models with different masses and angular momenta. We find that in all cases, viscosity drives the cores to rigid rotation and transports angular momentum outwards into the envelope. As a result, the core contracts in a quasi-stationary manner, and the outer layers expand to form a differentially rotating torus. Of the four models we have studied, the star with the highest mass collapses to a black hole, with about 20% of the rest mass leftover to form a massive accretion disk. On the contrary, the other three stars do not collapse to black holes, but form star + disk systems, similar to the final state of the rapidly rotating non-hypermassive neutron stars described above. As will be discussed in Section IIF, viscosity generates heat so that the stars do not evolve adiabatically in gen-

eral. The extra thermal pressure due to viscous heating helps to support the stars. We also consider the limit of rapid cooling, whereby the heat generated by viscosity is immediately removed from the stars. Of the three stars which do not collapse to black holes in the no-cooling limit, we found that the one with the lowest angular momentum undergoes catastrophic collapse in the rapid-cooling limit. About 10% of the rest mass is leftover to form an accretion disk in this case. To test the validity of the axisymmetric results, we perform 3D simulations to check for any nonaxisymmetric instabilities. We do not find any unstable nonaxisymmetric modes and the 3D results agree with the axisymmetric results.

Our results suggest that viscous braking of differential rotation in a hypermassive neutron star can, but does not always, lead to catastrophic collapse. When catastrophic collapse does occur, the remnant is a black hole surrounded by a massive accretion disk. This outcome is very different from that of the collapse of an unstable, rigidly-rotating “supramassive” neutron star, in which the whole star collapses to a black hole, leaving only a tiny amount of material to form a disk [20, 21]. Many models for GRBs require a massive disk around a rotating black hole to supply energy by neutrino processes [22]. Our results suggest that viscous forces in a hypermassive star could lead to the formation of a massive disk around such a black hole.

The structure of this paper is as follows. In Section II, we derive the relativistic Navier-Stokes equations containing shear viscosity in a 3+1 form suitable for numerical integration, and describe how we evolve them in both axisymmetry and full 3+1 dimensions. We then describe in Section III several tests that we perform to check our code. We present the results of our simulations on five selected stars in Section IV. Finally, we briefly summarize and discuss our conclusions in Section V.

II. FORMALISM AND NUMERICAL METHODS

A. Evolution of the gravitational fields

Throughout this paper, Latin indices denote spatial components (1-3) and Greek indices denote spacetime components (0-3). We adopt geometrized units, so that $G = c = 1$. We evolve the 3-metric γ_{ij} and the extrinsic curvature K_{ij} using the BSSN formulation [23]. The fundamental variables for BSSN evolution are

$$\phi \equiv \frac{1}{12} \ln[\det(\gamma_{ij})], \quad (1)$$

$$\tilde{\gamma}_{ij} \equiv e^{-4\phi} \gamma_{ij}, \quad (2)$$

$$K \equiv \gamma^{ij} K_{ij}, \quad (3)$$

$$\tilde{A}_{ij} \equiv e^{-4\phi} (K_{ij} - \frac{1}{3} \gamma_{ij} K), \quad (4)$$

$$\tilde{\Gamma}^i \equiv -\tilde{\gamma}^{ij}{}_{,j}. \quad (5)$$

The evolution and constraint equations for these fields are summarized in [24] (hereafter Paper I). In the presence of matter, these evolution equations contain the following source terms:

$$\begin{aligned}\rho &= n_\alpha n_\beta T^{\alpha\beta}, \\ S_i &= -\gamma_{i\alpha} n_\beta T^{\alpha\beta}, \\ S_{ij} &= \gamma_{i\alpha} \gamma_{j\beta} T^{\alpha\beta},\end{aligned}\quad (6)$$

where $T^{\alpha\beta}$ is the stress tensor, and $n_\alpha = (-\alpha, 0, 0, 0)$ is the future-directed unit normal to the time slice. One must impose gauge conditions which specify the lapse α and the shift β^i . We use a K-driver lapse and Gamma-driver shift, as described in Paper I. The numerical implementation of the equations is discussed in Paper I, with some improvements to enhance stability described in [25]. The latter are particularly relevant for the post-collapse version of our code that we implement with black-hole excision.

B. 3+1 relativistic Navier-Stokes equations

We treat the matter in our neutron stars as an imperfect fluid with a shear viscosity, but no bulk viscosity and no heat conduction. The stress tensor for the fluid is

$$T_{\mu\nu} = (\rho_0 + \rho_0\epsilon + P)u_\mu u_\nu + P g_{\mu\nu} - 2\eta\sigma_{\mu\nu}. \quad (7)$$

Here, ρ_0 , ϵ , P , and u_μ are the rest-mass density, specific internal energy, pressure, and fluid four-velocity, respectively. The quantity η is the coefficient of viscosity and is related to the kinematic viscosity ν by $\eta = \rho_0\nu$. The shear tensor $\sigma_{\mu\nu}$ is defined by [26]

$$\sigma_{\mu\nu} \equiv u_{(\mu;\nu)} + a_{(\mu}u_{\nu)} - \frac{1}{3}u^\alpha{}_{;\alpha}(g_{\mu\nu} + u_\mu u_\nu), \quad (8)$$

where a^μ is the fluid 4-acceleration. We assume a Γ -law equation of state

$$P = (\Gamma - 1)\rho_0\epsilon. \quad (9)$$

Our fundamental fluid variables are

$$\rho_\star \equiv \rho_0\alpha u^0 e^{6\phi}, \quad (10)$$

$$e_\star \equiv (\rho_0\epsilon)^{1/\Gamma} \alpha u^0 e^{6\phi}, \quad (11)$$

$$\tilde{S}_k \equiv \rho_\star h u_k, \quad (12)$$

where $h = 1 + \epsilon + P/\rho_0$ is the specific enthalpy. The conservation of stress-energy

$$T^{\mu\nu}{}_{;\nu} = 0 \quad (13)$$

and the law of baryon number conservation

$$\nabla_\mu(\rho_0 u^\mu) = 0 \quad (14)$$

give the relativistic continuity, energy, and Navier-Stokes equations

$$\partial_t \rho_\star + \partial_i(\rho_\star v^i) = 0 \quad (15)$$

$$\partial_t e_\star + \partial_i(e_\star v^i) = \frac{2}{\Gamma} \alpha e^{6\phi} \eta (\rho_0 \epsilon)^{(1-\Gamma)/\Gamma} \sigma^{\alpha\beta} \sigma_{\alpha\beta} \quad (16)$$

$$\begin{aligned}\partial_t \tilde{S}_k + \partial_i(\tilde{S}_k v^i) &= -\alpha e^{6\phi} P_{,k} + 2(\alpha e^{6\phi} \eta \sigma_k^\mu)_{,\mu} \\ &+ \alpha e^{6\phi} g^{\alpha\beta}{}_{,k} \left(\eta \sigma_{\alpha\beta} - \frac{1}{2} \rho_0 h u_\alpha u_\beta \right),\end{aligned}\quad (17)$$

where $v^i = u^i/u^0$ is the 3-velocity. The quantity u^0 is determined by the normalization condition $u^\nu u_\nu = -1$, which yields

$$w^2 = \rho_\star^2 + e^{-4\phi} \tilde{\gamma}^{ij} \tilde{S}_i \tilde{S}_j \left[1 + \frac{\Gamma e_\star^\Gamma}{\rho_\star (w e^{6\phi} / \rho_\star)^{\Gamma-1}} \right]^{-2}, \quad (18)$$

where $w = \rho_\star \alpha u^0$.

The stress-tensor $T^{\mu\nu}$ generates the following source terms in the field evolution equations:

$$\rho = h w e^{-6\phi} - P \quad (19)$$

$$-\frac{2\eta}{\alpha^2} (\sigma_{tt} - 2\sigma_{ti}\beta^i + \sigma_{ij}\beta^i\beta^j),$$

$$S_i = e^{-6\phi} \tilde{S}_i - \frac{2\eta}{\alpha} (\sigma_{ti} - \sigma_{ij}\beta^j), \quad (20)$$

$$S_{ij} = \frac{e^{-6\phi}}{w h} \tilde{S}_i \tilde{S}_j + P \gamma_{ij} - 2\eta \sigma_{ij}. \quad (21)$$

C. 2+1 relativistic Navier-Stokes equations

Many of the systems we evolve possess and maintain symmetry about their rotation axis, which we set to be the z -axis. Then we can eliminate one dimension and simplify the equations. We utilize axisymmetry and follow [27, 28] to evolve the field and hydrodynamic variables on the $y = 0$ plane. The data off of this plane can be obtained by rotating the data on this plane. As we explain in Section II G 1, we find it advantageous when performing 2+1 simulations to evolve the hydrodynamic equations (15)-(17) in cylindrical coordinates but on a Cartesian (xz) grid. On the $y = 0$ plane, the cylindrical coordinates $\varpi = \sqrt{x^2 + y^2}$, z , and $\varphi = \arctan(y/x)$ are related to the Cartesian coordinates x , y , and z as follows: $\varpi \leftrightarrow x$, $\varpi\varphi \leftrightarrow y$, $z \leftrightarrow z$. Using these relations,

Eqs. (15)-(17) in cylindrical coordinates can be written

$$\partial_t \rho_\star + \frac{1}{x} \partial_B (\rho_\star x v^B) = 0 \quad (22)$$

$$\begin{aligned} \partial_t (\tilde{S}_A - 2\alpha e^{6\phi} \eta \sigma_A^0) + \frac{1}{x} \partial_B (x \tilde{S}_A v^B - 2x\alpha e^{6\phi} \eta \sigma_A^B) \\ = \frac{1}{x} (\tilde{S}_y v^y - 2x\alpha e^{6\phi} \eta \sigma_y^y) \delta_{Ax} - \alpha e^{6\phi} \partial_A P \end{aligned} \quad (23)$$

$$\begin{aligned} + \alpha e^{6\phi} g^{\alpha\beta}{}_{,A} \left[-\frac{1}{2} \rho_0 h u_\alpha u_\beta + \eta \sigma_{\alpha\beta} \right] \\ \partial_t (\tilde{S}_y - 2\alpha e^{6\phi} \eta \sigma_y^0) \end{aligned} \quad (24)$$

$$\begin{aligned} + \frac{1}{x^2} \partial_B (x^2 \tilde{S}_y v^B - 2\alpha e^{6\phi} \eta x^2 \sigma_y^A) = 0 \\ \partial_t e_\star + \frac{1}{x} \partial_B (e_\star x v^B) \\ = \frac{2}{\Gamma} \alpha e^{6\phi} \eta (\rho_0 \epsilon)^{(1-\Gamma)/\Gamma} \sigma^{\alpha\beta} \sigma_{\alpha\beta} , \end{aligned} \quad (25)$$

where the indices A and B run over x and z (c.f. Eq.(2.10)-(2.13) of [28]).

D. Hierarchy of timescales

There are two dynamical timescales for a rotating star. Gravity provides the free-fall timescale τ_{FF}

$$\tau_{\text{FF}} \sim \left(\frac{R^3}{M} \right)^{1/2} \sim 10^{-4} \left(\frac{M/R}{0.2} \right)^{-3/2} \left(\frac{M}{2M_\odot} \right) \text{ s} , \quad (26)$$

where M is the gravitational mass of the star (or merged binary remnant) and R is the radius. If the star is rotating, its rotation period P_{rot} provides another important timescale:

$$P_{\text{rot}} = \frac{2\pi}{\Omega} = 1.6 \times 10^{-3} \left(\frac{\Omega}{4000\text{s}^{-1}} \right)^{-1} \text{ s} . \quad (27)$$

Dynamical instabilities (e.g. instability to radial collapse or to dynamical bar formation) will act on the above timescales.

The stars we study are dynamically stable initially, so their structure is altered on secular timescales. Rotating compact stars may be secularly unstable to gravitational-radiation driven instabilities. The strongest instabilities of this kind are the (nonaxisymmetric) r -modes and the bar mode. The timescale of the $l = m = 2$ r -mode instability is given by [4]

$$\tau_r^{\text{GW}} \sim 50 \left(\frac{\Omega}{4000\text{s}^{-1}} \right)^{-6} \left(\frac{M/R}{0.2} \right)^4 \left(\frac{M}{2M_\odot} \right)^{-5} \text{ s} . \quad (28)$$

The gravitational-radiation driven (Dedekind) bar-mode instability occurs if the star is rapidly rotating so that $T/|W| > \beta_s$, where $T/|W|$ is the ratio of kinetic to gravitational potential energy. The threshold $\beta_s \approx 0.14$ for a Newtonian star ($M/R \ll 1$), and *decreases* as the

compactness of the star (i.e. M/R) increases [29]. The timescale of this instability is estimated to be [30]

$$\tau_{\text{bar}}^{\text{GW}} \sim 0.1 \left(\frac{M/R}{0.2} \right)^{-4} \left(\frac{M}{2M_\odot} \right) \left(\frac{T/|W| - \beta_s}{0.1} \right)^{-5} \text{ s} . \quad (29)$$

Viscosity alone can also drive a (Jacobi) bar-mode instability. The threshold is identical for a Newtonian star ($\beta_s \approx 0.14$) but *increases* as the compaction increases [3]. The relevant timescale is (see [1], p.99)

$$\tau_{\text{bar}}^{\text{vis}} \sim \frac{R^2}{4\nu} \left(\frac{T/|W| - \beta_s}{0.1} \right)^{-1} \text{ s} . \quad (30)$$

This is comparable to the viscous timescale $\tau_{\text{vis}} \sim R^2/\nu$ discussed below.

Magnetic fields coupled to the matter will redistribute angular momentum. In fact, even an initially small magnetic field frozen into the matter will be wound up and can destroy differential rotation in the star on an Alfvén timescale [7, 12, 15]:

$$\tau_B \sim 100 \left(\frac{B}{10^{12}\text{G}} \right)^{-1} \left(\frac{M/R}{0.2} \right)^{1/2} \text{ s} . \quad (31)$$

Viscosity will also redistribute angular momentum on a viscous timescale τ_{vis} . One form of viscosity present in neutron stars is due to the transport of energy and momentum of neutrons. This viscosity acts on a timescale [31, 32]

$$\tau_{n,\text{vis}} \sim 10^8 T_9^2 \left(\frac{M}{2M_\odot} \right)^{9/2} \left(\frac{M/R}{0.2} \right)^{-23/4} \text{ s} , \quad (32)$$

where $T_9 = T/10^9\text{K}$, and T is the characteristic temperature.

It is widely believed that, for cold neutron stars ($T \lesssim 10^9\text{K}$), the neutron fluid in the inner crust condenses into a superfluid of 1S_0 Cooper pairs [33], while in the interior, the neutrons could form a 3P_2 superfluid [34] (although this is less certain), and the protons a 1S_0 superfluid. In the case of neutron superfluidity, $\tau_{n,\text{vis}}$ will vanish, and the dominant viscosity will be due to electron-electron scattering [32, 35]

$$\tau_{e,\text{vis}} \sim 10^8 T_9^2 \left(\frac{M}{2M_\odot} \right)^4 \left(\frac{M/R}{0.2} \right)^{-5} \text{ s} . \quad (33)$$

Electron and proton fluids are forced to move together in the MHD limit [36]. Differences in velocity between the neutron and proton-electron fluids are damped fairly quickly by mutual friction [36, 37].

Viscosity can be used as a model for turbulence in certain situations. Turbulence may occur in young neutron stars as a result of pure hydrodynamic effects or magnetic instabilities [16]. Turbulence is often modeled by the “ α -disk” law, in which a shear stress $T_{\varpi\varphi} = -\alpha P$ is added to the hydrodynamic equation (see e.g. [38], Chap. 14).

Here α is a nondimensional constant (which should not be confused with the lapse function) with values in the range $0.001 \lesssim \alpha \lesssim 1$. The viscosity in this model roughly corresponds to $\nu \sim l_{\text{turb}} v_{\text{turb}} \sim \alpha R c_s$, where v_{turb} is the velocity of turbulent cells relative to the mean fluid motion, l_{turb} is the size of the largest turbulent cell, and c_s is the sound speed. The corresponding timescale is

$$\tau_{\text{vis}}^{\text{turb}} \sim \frac{1}{\alpha} \tau_{\text{FF}} \sim \frac{10^{-4}}{\alpha} \left(\frac{M/R}{0.2} \right)^{-3/2} \left(\frac{M}{2M_{\odot}} \right) \text{ s}, \quad (34)$$

which is much shorter than all the other secular timescales. Hence turbulent viscosity, if present, is likely to dominate the secular evolution of differentially rotating stars.

Thermal energy is radiated away primarily by neutrinos. For hot neutron stars ($T \gtrsim 10^9 K$), the cooling is dominated by the direct URCA process, and the star cools on a timescale $\tau_{\text{cool}} \sim 10^2 T_9^{-4}$ s (see [39] and [38], Chap. 11). For cooler neutron stars, the cooling is dominated by the modified URCA process, and the star cools on a timescale $\tau_{\text{cool}} \sim 10^7 T_9^{-6}$ s [39]. Depending on the temperature and the nature of the viscosity, the cooling timescale may be greater than or less than the viscous timescale. If $\tau_{\text{vis}} \ll \tau_{\text{cool}}$, then the heat generated by viscosity will build up inside the star. Otherwise, it will be radiated away as quickly as it is generated. We study both limits in this paper.

E. Dynamically modeling secular effects

Secular effects will in general take many rotation periods to significantly affect the structure or velocity profile of a differentially rotating star. This poses a challenge to the numerical treatment of these changes. Because of the short Courant timestep required for numerical stability, it would be computationally prohibitive to evolve a star for such a long time using an explicit finite differencing scheme. The use of a fully implicit scheme for the finite differencing can allow stable evolutions with larger ΔT . Each timestep is, however, much more computationally expensive as it involves matrix inversion. Moreover, no fully implicit routine for the coupled Einstein field and relativistic hydrodynamic equations exists at present.

The secular timescales are so much longer than the dynamical timescales that the star can be thought of as evolving quasi-statically. Therefore, it might be possible to treat the secular evolution in the quasistatic approximation, as in typical stellar evolution (Heney) codes, by constructing a sequence of equilibrium configurations up to the moment that stable equilibrium can no longer be sustained. This approach has been used to study the viscous evolution of differentially rotating white dwarfs [40]. However, building the required equilibrium models in full general relativity is a nontrivial task. It would be particularly difficult to identify the meridional currents and core-halo bifurcation that often arise in rapidly rotating

configurations. More significantly, it would not be possible to follow the evolution of the configuration with a quasistationary approach if a dynamical instability (i.e. collapse) is triggered during the secular evolution.

Instead, we use our relativistic hydrodynamic code and artificially amplify the strength of viscosity so that the viscous timescale is short enough to make numerical treatment tractable. However, we keep the viscous timescale sufficiently long that the hierarchy of timescales is maintained, and the secular evolution still proceeds in a quasi-stationary manner. The behavior of the real system can then be determined by rescaling the time variable to adjust the viscous timescale to its physical value. The characteristic viscous timescale is

$$\tau_{\text{vis}} \sim \rho R^2 \langle \eta \rangle^{-1}, \quad (35)$$

where $\langle \eta \rangle$ is an averaged value of η across the star. Suppose we evolve the same star, once with $\tau_{\text{vis}} = \tau_1$ and once with $\tau_{\text{vis}} = \tau_2$. If both τ_1 and τ_2 are large enough so that they do not compete with the dynamical timescale, but shorter than any other secular timescale (see, e.g. Section II D), then the configuration of the star with viscosity τ_1 at time t will be the same as the configuration of the star with viscosity τ_2 at time $(\tau_2/\tau_1)t$. By varying τ_{vis} over a wide range and corroborating this scaling, we are confident that the physical behavior we observe is real. We can then scale the result of numerical simulations to the appropriate strength of viscosity, provided that the physically relevant viscous timescale is much shorter than all the other secular timescales (e.g., $\tau_r^{\text{GW}}, \tau_{\text{bar}}^{\text{GW}}$).

As discussed in the previous subsection, turbulent viscosity is likely to dominate the secular evolution. We adopt the stress tensor as in Eq. (7) and specify the viscosity η suitable for modeling turbulence. We consider the turbulent viscosity described in [41]:

$$\eta \sim \rho l_{\text{turb}} v_{\text{turb}}. \quad (36)$$

(This viscosity law is also used in some accretion-disk models [16].) Typically, v_{turb} is proportional to the sound speed c_s . Hence $\eta \sim l_{\text{turb}} \rho \sqrt{P/\rho} \sim (l_{\text{turb}}/c_s) P$. For simplicity, we assume that l_{turb}/c_s is constant inside the star. Then we have

$$\eta = \nu_P P, \quad (37)$$

where ν_P is a constant, and is related to the coefficient of kinematic viscosity ν by $\nu_P = (\rho_0/P)\nu$. In our numerical simulations we specify the value of ν_P for each run.

We model the initial stars as rotating polytropes with polytropic index $n = 1$, so that $P = \kappa \rho_0^2$. It is convenient to rescale all quantities with respect to κ . Since $\kappa^{1/2}$ has dimensions of length, we can define the following nondimensional variables [47]

$$\bar{x}^\mu = \kappa^{-1/2} x^\mu, \quad \bar{\Omega} = \kappa^{1/2} \Omega, \quad (38)$$

$$\bar{M} = \kappa^{-1/2} M, \quad \bar{R} = \kappa^{-1/2} R, \quad (39)$$

$$\bar{\rho}_0 = \kappa \rho_0, \quad \bar{\nu}_P = \kappa^{-1/2} \nu_P, \quad (40)$$

where the spacetime coordinates are $x^\mu = (t, x, y, z)$. However, to simplify our notation, we will drop all the bars. Hereafter, all variables are understood to be in “ $\kappa = 1$ units.”

Using Eq. (35), we can see that τ_{vis} scales with R , ρ , and ν_P as

$$\tau_{\text{vis}} \sim \frac{R^2}{\nu} \sim \frac{R^2 \rho}{\nu_P P} \quad (41)$$

which for $n = 1$ becomes

$$\tau_{\text{vis}} \sim \frac{R^2}{\rho \nu_P}. \quad (42)$$

For definiteness, we take τ_{vis} to be

$$\tau_{\text{vis}} = \lambda \frac{R_{\text{eq}}^2}{\rho_{0,\text{max}} \nu_P}, \quad (43)$$

where R_{eq} is the equatorial radius, $\rho_{0,\text{max}}$ is the maximum value of ρ_0 in the star, and λ is a dimensionless constant. We use the constant λ to approximately match τ_{vis} to the rate of decay of differential rotation observed by our simulations. With the appropriate τ_{vis} , the value of $\sigma_{\mu\nu} \sigma^{\mu\nu}$, which is proportional to the rate of energy dissipation [see Eq. (16)], is expected to decay like

$$\sigma_{\mu\nu} \sigma^{\mu\nu} \approx (\sigma_{\mu\nu} \sigma^{\mu\nu})|_{t=0} \exp(-2t/\tau_{\text{vis}}). \quad (44)$$

We measure τ_{vis} by numerically evolving a given star, and observing the decay with time of $\langle \sigma^{\mu\nu} \sigma_{\mu\nu} \rangle$, the average value of $\sigma^{\mu\nu} \sigma_{\mu\nu}$ throughout the star, weighted by rest density. We determine the value of λ by requiring that τ_{vis} roughly corresponds to the e-folding time of the decay of $\sqrt{\langle \sigma^{\mu\nu} \sigma_{\mu\nu} \rangle}$. Carrying out this measurement on a sampling of the stars used below, we find that $\lambda \approx 0.23$ in all cases. Thus we use $\lambda = 0.23$ to define τ_{vis} in the sections below.

We note that the turbulent viscosity adopted above for our numerical treatment is roughly equivalent to an “ α ” model provided we identify $\alpha \sim (c_s/R) \nu_P \sim (M/R^3)^{1/2} \nu_P$. Eq. (43) for τ_{vis} is then equivalent to Eq. (34).

F. Radiative cooling

Our stars do not evolve isentropically. Viscosity heats the matter on a timescale τ_{vis} , as shown by Eq. (16). At the same time, neutrino radiation carries away heat, cooling the star on a timescale τ_{cool} . We will carry out simulations below in two opposite limits, which we describe in some detail in Appendix A. In the *no-cooling* limit, $\tau_{\text{cool}} \gg \tau_{\text{vis}}$, so we ignore radiative cooling and simply evolve Eqs. (15)-(17). In the *rapid-cooling* limit, $\tau_{\text{cool}} \ll \tau_{\text{vis}}$, so we evolve Eqs. (15)-(17) as before, but *without including* the viscous heating term in the energy equation [Eq. (16)]. This will allow net heating by adiabatic compression but not by viscosity. The viscous heat

is assumed to be (instantaneously) lost by radiation in this limit, while viscous braking proceeds. The emitted radiation will carry off some momentum as well as energy, causing a modification of Eq. (17), but this will have a much smaller effect provided the luminosity does not exceed the (neutrino) Eddington luminosity. Baumgarte and Shapiro [42] investigated the loss of angular momentum in binary neutron star merger remnants due to radiation, and they found it to be fairly small. We therefore feel justified in ignoring radiative corrections to Eq. (17).

G. Numerical Implementation

1. 2+1 Dimensional Code

Our hydrodynamical scheme employs Van Leer-type advection with artificial viscosity to handle shocks. We also use a “no-atmosphere” approach, in which the density at any point on our grid can fall exactly to zero. Our hydrodynamical algorithms are described in detail in Paper I. We have evolved the above equations both in two dimensions, assuming axisymmetry, and in three dimensions. Using axisymmetry saves us computational time and allows us to use higher resolution. However, 3D runs must still be carried out for rapidly rotating systems in order to check for the occurrence of nonaxisymmetric instabilities. There are several ways to evolve in axisymmetry. One could write the field and hydrodynamic evolution equations in cylindrical coordinates (ϖ, z, φ) and evolve in this coordinate system. This has the advantage that one can explicitly remove the dependence of the variables on φ . Unfortunately, there are singularities in the cylindrical coordinate system which can make the evolution of the field equations in these coordinates difficult. Instead, we choose to evolve the metric variables $(\tilde{\gamma}_{ij}, \tilde{A}_{ij}, \phi, K, \tilde{\Gamma}^i, \alpha, \text{ and } \beta^i)$ in axisymmetry using the Cartoon method [27]. In this approach, variables are evolved on a Cartesian grid consisting of three planes corresponding to $y = -\Delta Y$, $y = 0$, and $y = \Delta Y$. Then the middle ($y = 0$) plane is evolved using the 3D evolution equations in Cartesian coordinates. Each time the middle plane is evolved forward one timestep, the $y = -\Delta Y$ and $y = \Delta Y$ planes are updated by applying the assumption of axisymmetry. Thus, the value of a tensor \mathbf{f} at location $(\varpi, z, \pm\varphi)$ on $y = \pm\Delta Y$ is equal to \mathbf{f} at $(\varpi, z, 0)$ rotated by (coordinate) tensor transformation about the z -axis by angles $\pm\varphi$. Since an arbitrary point $(\varpi, z, 0)$ will generally not coincide with any gridpoint on the $y = 0$ plane, interpolation in x is necessary to apply this update. We use third-order polynomial interpolation, so that we do not lose second-order accuracy.

With the hydrodynamic evolution equations, we also have the choice of either evolving in cylindrical coordinates or evolving in Cartesian coordinates using the Cartoon prescription. Like Shibata in his work on axisymmetric star collapse [28, 43], we choose to evolve the fluid

variables in cylindrical coordinates, i.e. we use Eqs. (22)-(25). This is superior to using the Cartoon method because Eq. (22) can be finite differenced in such a way that the total rest mass will be exactly conserved (except for flow beyond the outer boundaries). In the absence of viscosity, angular momentum also becomes a numerically conserved quantity. We have found that evolving the fluid variables in cylindrical coordinates gives significantly more accurate runs than evolving via Cartoon hydrodynamics. The drawback of using 2D evolutions is the instability caused by the coordinate singularity on the $x = 0$ axis. (This instability is also present if we use the 3D Cartesian Navier-Stokes equations together with the Cartoon boundary condition.) There are several ways of removing this instability. Shibata [28] adds a small artificial shear viscosity

$$\partial_t(\tilde{S}_A/\rho_\star) = \dots + \nu_{\text{art}}\rho_\star\Delta(\tilde{S}_A/\rho_\star), \quad (45)$$

where Δ is the flat-space Laplacian, and $\tilde{S}_i/\rho_\star = hu_i$ is the momentum variable evolved by the code of [28] (instead of \tilde{S}_i).

We have confirmed that adding such a term to Eq. (17) can stabilize our code. However, since we will be studying the effects of real shear viscosity, we instead choose to remove the instability using a higher-order dissipation scheme. Namely, we add a small Kreiss-Oliger dissipation term [44]

$$\partial_t\tilde{S}_A = \dots - C_{\text{ko}}\frac{(\Delta X\Delta Z)^2}{16\Delta T}\Delta^2\tilde{S}_A, \quad (46)$$

We use $C_{\text{ko}} = 0.2$ for all the simulations reported in this paper.

In both 2D and 3D simulations, we assume that our system preserves equatorial symmetry across the $z = 0$ plane, and we therefore only evolve the $z > 0$ portion of the grid. In 3D runs, we make the added assumption of π -symmetry, which allows us to evolve only half of the remaining grid, which we choose to be the $y > 0$ half. When performing 2D runs, we evolve only the region $x > 0$ since the values of variables in the $x < 0$ region can be deduced from the values on the $x > 0$ region from the assumed axisymmetry.

2. Finite differencing

We compute all spacial derivatives using standard centered differencing. We integrate forward in time using a 3-step iterated Crank-Nicholson scheme. So, for example, we evolve the equation $\partial_t f = \dot{f}(f)$ from timestep n at time t to timestep $n+1$ at time $t+\Delta T$ by the following algorithm:

- (i) **Predict:** ${}^1f^{n+1} \equiv f^n + \Delta T\dot{f}(f^n)$
- (ii) **1st Correct:**
 ${}^2f^{n+1} \equiv f^n + \Delta T[0.4\dot{f}(f^n) + 0.6\dot{f}({}^1f^{n+1})]$
- (iii) **2nd Correct:**
 $f^{n+1} = f^n + \Delta T[0.4\dot{f}(f^n) + 0.6\dot{f}({}^2f^{n+1})]$

As discussed in Paper I, the coefficients 0.4 and 0.6 were chosen to improve stability.

In the presence of viscosity, the time-differencing is not entirely straightforward, due to the presence of time derivatives of u_μ in $\sigma_{\mu\nu}$, and of time derivatives of $\sigma_{\mu\nu}$ in the Navier-Stokes equations. Thus, $\partial_t\tilde{S}_k$ (which gives $\partial_t u_k$) is an expression which itself contains $\partial_t u_k$ and $\partial_t^2 u_k$. Since the viscosity is a small perturbing force on the fluid motion, we find that it is sufficient to split off the viscous terms and integrate them separately (operator splitting). In particular, we compute $\partial_t u_k$ and $\partial_t\sigma_k^0$ appearing in the viscous terms in a non-time centered way. Consider the \tilde{S} evolution equation for the viscous piece: $\partial_t\tilde{S} = \dot{\tilde{S}}(\sigma, \dot{\sigma})$, where we have suppressed all indices. To evolve this equation from timestep n to timestep $n+1$, we need to know the time derivatives of u and σ . When performing the predictor step, these time derivatives are approximated by subtracting values of the fields on the timestep n from those on the previous timestep, $n-1$.

- (i) **Before predictor step,**
compute $\dot{u}^{n-1/2} = [u^n - u^{n-1}]/\Delta T$,
 $\sigma^n = \sigma(u^n, \dot{u}^{n-1/2})$,
 $\dot{\sigma}^{n-1/2} = [\sigma^n - \sigma^{n-1}]/\Delta T$

Note that these time derivatives are centered at $n-1/2$. We then carry out the predictor step.

- (ii) **Predict:** ${}^1\tilde{S}^{n+1} = \tilde{S}^n + \Delta T\dot{\tilde{S}}(\sigma^n, \dot{\sigma}^{n-1/2})$

From the predicted values of u and σ , we construct time derivatives centered at $n+1/2$ and use these in the corrector step.

- (iii) **compute ${}^1u^{n+1}$ from ${}^1\tilde{S}^{n+1}$**
 ${}^1\dot{u}^{n+1/2} = [{}^1u^{n+1} - u^n]/\Delta T$,
 ${}^1\sigma^{n+1} = \sigma({}^1u^{n+1}, {}^1\dot{u}^{n+1/2})$,
 ${}^1\dot{\sigma}^{n+1/2} = [{}^1\sigma^{n+1} - \sigma^n]/\Delta T$
- (iv) **1st Correct:**
 ${}^2\tilde{S}^{n+1} = \tilde{S}^n + \Delta T[0.4\dot{\tilde{S}}(\sigma^n, \dot{\sigma}^{n-1/2}) + 0.6\dot{\tilde{S}}({}^1\sigma^{n+1}, {}^1\dot{\sigma}^{n+1/2})]$
- (iii) **compute ${}^2u^{n+1}$ from ${}^2\tilde{S}^{n+1}$**
 ${}^2\dot{u}^{n+1/2} = [{}^2u^{n+1} - u^n]/\Delta T$,
 ${}^2\sigma^{n+1} = \sigma({}^2u^{n+1}, {}^2\dot{u}^{n+1/2})$,
 ${}^2\dot{\sigma}^{n+1/2} = [{}^2\sigma^{n+1} - \sigma^n]/\Delta T$
- (iv) **2nd Correct:**
 $\tilde{S}^{n+1} = \tilde{S}^n + \Delta T[0.4\dot{\tilde{S}}(\sigma^n, \dot{\sigma}^{n-1/2}) + 0.6\dot{\tilde{S}}({}^2\sigma^{n+1}, {}^2\dot{\sigma}^{n+1/2})]$

By differencing the equations in this way, the dominant nonviscous terms in the evolution equations are accurate to second order (except for small effects due to the use of the coefficients 0.4 and 0.6 in the corrector steps), but small viscous terms involving time derivatives are only accurate to first order in ΔT . Numerical convergence tests show that our code is nearly second-order convergent in space and time. We find this to be sufficient for our purposes. When computing $\sigma_{\mu\nu}$, we first use Eq. (8) to get the spatial components σ_{ij} . The remaining components $\sigma_{0\mu}$ are then obtained from the conditions $u^\mu\sigma_{\mu\nu} = 0$.

As in most other Eulerian hydrodynamic codes, high

velocities can easily develop in the low-density regions near the surfaces of our stars. The method for evolving such regions in the absence of viscosity is described in Paper I. Since calculation of the shear tensor involves taking derivatives of the velocity field, we are unable to calculate it accurately in the very low-density regions. To ensure stability, we set $\eta = 0$ in regions where $\rho_0 < 10^{-3}\rho_{0,\text{max}}$. Since these low-density regions contain an insignificant amount of rest mass, this prescription should not affect our evolutions. We confirm this by varying the cutoff density in several test problems and checking that the effect is negligible.

H. Diagnostics

Our most important diagnostics are the total mass-energy M and angular momentum J . These are both defined by surface integrals at infinity [45]:

$$M = \frac{1}{16\pi} \int_{S_\infty} \sqrt{\gamma} \gamma^{im} \gamma^{jn} (\gamma_{mn,j} - \gamma_{jn,m}) d^2 S_i \quad (47)$$

$$J_i = \frac{1}{8\pi} \varepsilon_{ij}{}^k \int_{S_\infty} x^j K_k^m d^2 S_m. \quad (48)$$

Using Gauss' Law, these surface integrals can be converted to volume integrals:

$$M = \int_V \left(e^{5\phi} \left(\rho + \frac{1}{16\pi} \tilde{A}_{ij} \tilde{A}^{ij} - \frac{1}{24\pi} K^2 \right) \right. \quad (49)$$

$$\left. - \frac{1}{16\pi} \tilde{\Gamma}^{ijk} \tilde{\Gamma}_{jik} + \frac{1 - e^\phi}{16\pi} \tilde{R} \right) d^3 x$$

$$J_i = \varepsilon_{ij}{}^k \int_V \left(\frac{1}{8\pi} \tilde{A}_k^j + x^j S_k \right. \quad (50)$$

$$\left. + \frac{1}{12\pi} x^j K_{,k} - \frac{1}{16\pi} x^j \tilde{\gamma}^{lm}{}_{,k} \tilde{A}_{lm} \right) e^{6\phi} d^3 x.$$

In axisymmetry, the angular momentum integral simplifies to [46]

$$J_z = \int_V x S_y d^3 x. \quad (51)$$

Henceforth, we drop the subscript z since all angular momentum is in the z -direction.

The mass M and angular momentum J in our grid should be strictly conserved only in the absence of radiation (although gravitational radiation carries no angular momentum in axisymmetry). Since the energy and angular momentum emitted in gravitational waves are negligible in our runs, this means that M and J should be conserved in the no-cooling limit. They thus serve as useful code checks in this limit. In the rapid-cooling limit, the mass computed by the volume integral (49) over the numerical grid will not be conserved—thermal energy is carried off of the grid by thermal radiation. The expected rate of mass-energy decrease due to thermal energy loss can be computed by differentiating Eq. (49) with respect

to time. To lowest order, we can ignore the effects of the quasi-stationary loss of thermal energy on the spacetime, and so ignore the time derivatives of field variables. Then only the first term in Eq. (49) will be important.

$$\left. \frac{dM}{dt} \right|_{\text{cooling}} = \frac{d}{dt} \int_V d^3 x e^{5\phi} \rho + \dots$$

$$\approx \int_V d^3 x e^{5\phi} \left. \frac{\partial \rho}{\partial t} \right|_{\text{cooling}}, \quad (52)$$

where $\partial \rho / \partial t|_{\text{cooling}}$ is the component of the time derivative of ρ caused by loss of internal energy due to cooling. This quantity may be computed by applying the chain rule to Eq. (19):

$$\left. \frac{dM}{dt} \right|_{\text{cooling}} = \int_V \left. \frac{\partial \rho}{\partial \epsilon} \right|_{\rho_0, u^0} \left. \frac{\partial \epsilon}{\partial e_\star} \right|_{\rho_0, u^0} \left. \frac{\partial e_\star}{\partial t} \right|_{\text{cooling}} e^{5\phi} d^3 x. \quad (53)$$

Changes in u^0 are ignored because they represent a higher-order influence on dM/dt . The rate of change in e_\star due to cooling is given by the effective balance of heating and cooling that characterizes the rapid-cooling limit (see Appendix A). Thus, $\partial_t e_\star|_{\text{cooling}}$ is minus the value of $\partial_t e_\star$ due to viscous heating, i.e.

$$\left. \frac{\partial e_\star}{\partial t} \right|_{\text{cooling}} = -\frac{2}{\Gamma} \alpha e^{6\phi} \eta (\rho_0 \epsilon)^{(1-\Gamma)/\Gamma} \sigma^{\alpha\beta} \sigma_{\alpha\beta} \quad (54)$$

[see Eq. (16)]. From equations (53) and (54), it is straightforward to construct

$$\left. \frac{dM}{dt} \right|_{\text{cooling}} = - \int_V d^3 x 2e^{5\phi} \alpha e^{6\phi} \eta \sigma^{\alpha\beta} \sigma_{\alpha\beta} \quad (55)$$

$$\times \left(\frac{\rho_0}{\rho_\star} \right) \left[\Gamma e^{-12\phi} \left(\frac{\rho_\star}{\rho_0} \right)^2 - \Gamma + 1 \right].$$

Finally, the quantity which is nearly conserved in the rapid-cooling limit (up to losses due to gravitational radiation) is

$$M_{\text{tot}} = M + M_{\text{cooling}} \equiv M - \int_0^t dt' \left. \frac{dM}{dt'} \right|_{\text{cooling}}. \quad (56)$$

In both the no-cooling and rapid-cooling runs, we can divide M into its constituent pieces: the rest mass M_0 , internal energy mass M_i , kinetic energy T , and gravitational potential energy W , defined by [47]

$$M_0 = \int_V \rho_0 d\mathcal{V} \quad (57)$$

$$M_i = \int_V (\rho_0 \epsilon) d\mathcal{V} \quad (58)$$

$$T = \int_V \frac{1}{2} \Omega T_\varphi^0 (u^0)^{-1} d\mathcal{V} \quad (59)$$

$$W = M - M_0 - M_i - T, \quad (60)$$

where $d\mathcal{V} = \alpha u^0 e^{6\phi} d^3 x$ is the proper 3-volume element. To study the effects of heating, it is useful to

break up the internal energy ϵ into its “cold” component $\epsilon_0 = \rho_0^{\Gamma-1}/(\Gamma-1)$, and its “thermal” component $\epsilon_{\text{heat}} = \epsilon - \epsilon_0$. Then we can break up M_i into cold and hot components

$$M_{ic} = \int_V (\rho_0 \epsilon_0) dV \quad (61)$$

$$M_{ih} = \int_V (\rho_0 \epsilon_{\text{heat}}) dV. \quad (62)$$

Note that in the rapid-cooling limit, $M_{ih} = 0$.

Finally, we also compute the circulation along closed curves. For a closed curve c with tangent vector λ^μ , the circulation is defined to be

$$\mathcal{C}(c) = \oint_c hu_\mu \lambda^\mu d\zeta, \quad (63)$$

where ζ parameterizes points on c [i.e. $\lambda^\mu = (\partial/\partial\zeta)^\mu$]. According to the Kelvin-Helmholtz theorem, the circulation \mathcal{C} will be conserved in the absence of viscosity if c moves with the fluid and if the fluid is barotropic [$P = P(\rho_0)$]. When viscosity is present or the equation of state is more general, as in the case of nonisentropic flow, the Navier-Stokes equations give

$$\frac{d\mathcal{C}}{d\tau} = - \oint_c \lambda^\mu \rho_0^{-1} \left[P_{,\mu} - 2(\eta\sigma_\mu{}^\nu)_{;\nu} \right] d\zeta. \quad (64)$$

If $\eta = 0$, the second term in the integrand vanishes, and if $P = P(\rho_0)$, the remaining term is an exact differential. Then $d\mathcal{C}/d\tau$ integrates to zero, in accord with the Kelvin-Helmoltz theorem.

In axisymmetry, we choose to evaluate \mathcal{C} on circular rings on the equatorial $z = 0$ plane, so that $\zeta = \varphi$. The ring c intersects our 2D grid at a point on the x -axis. By our symmetries, the curve c will always remain circular and always remain at $z = 0$, so the Lagrangian point representing c only moves in x . Evolution in t and in τ are simply related by $d/d\tau = u^0 d/dt$. Since the system is axisymmetric, the integrand, being a scalar, is constant along c , so Eqs. (63) and (64) simplify to

$$\mathcal{C} = 2\pi hu_\varphi = 2\pi h x u_y \quad (\text{axisym}) \quad (65)$$

$$\begin{aligned} \frac{d\mathcal{C}}{dt} &= \frac{1}{u^0} \frac{d\mathcal{C}}{d\tau} = \frac{4\pi}{\rho_0 u^0} (\eta\sigma_\varphi{}^\nu)_{;\nu} \\ &= \frac{4\pi}{\rho_\star x} \left[(x^2 \alpha e^{6\phi} \eta \sigma_y{}^0)_{,t} + (x^2 \alpha e^{6\phi} \eta \sigma_y{}^A)_{,A} \right] \end{aligned} \quad (66)$$

Hence the quantity \mathcal{C}_{tot} given by

$$\mathcal{C}_{\text{tot}} = \mathcal{C} + \mathcal{C}_{\text{vis}} \equiv \mathcal{C} - \int_0^t dt' \frac{d\mathcal{C}}{dt'} \quad (67)$$

is conserved, even in the presence of viscosity.

Finally, we compute the Hamiltonian and momentum constraint violations [given by equations (16) and (17) of Paper I]. We monitor the L2 norm of the violation of each

constraint. We compute the L2 norm of a gridfunction g by summing over every gridpoint i :

$$L2(g) = \sqrt{\sum_i g_i^2}. \quad (68)$$

The constraint violations are normalized as described in Paper I [Eqs. (59) and (60)].

III. CODE TESTS

In Paper I, we presented our relativistic hydrodynamic code. This code evolves the coupled Einstein field relativistic hydrodynamic system on 3D grids, assuming perfect-fluid hydrodynamics. We demonstrated the ability of our code to distinguish stable from unstable relativistic polytropes, to accurately follow gravitational collapse of rotating stars, and to accurately evolve binary polytropes in quasi-stationary circular orbits. When black holes appear on our grid, we can employ excision to remove the spacetime singularities from our grid. Tests of our black hole excision algorithm using this code were reported in [48] for single rotating black holes in vacuum spacetimes and in [25] for black holes that arise during the collapse of hydrodynamic matter. In this section, we test the adaptations of this code which force axisymmetric evolution and the modifications which allow a physical viscosity. Simulations performed with our axisymmetric code show that stable and unstable TOV stars are correctly distinguished. The code also achieves approximate second order convergence in the evolution of linear gravitational waves and TOV stars. Below, we describe test runs on rotating stars in some detail. First, we consider stable and unstable uniformly rotating stars, as well as a stable differentially rotating star, in axisymmetry and without viscosity. We then test the sensitivity of our code to nonaxisymmetric *dynamical* bar formation. Finally, we check that physical viscosity is implemented correctly by considering stable uniformly and differentially rotating models. A summary of the models used for these code tests is given in Table I. The models are initially $n = 1$ equilibrium polytropes and are evolved using a Γ -law equation of state with $\Gamma = 2$ [see Eq. (9)]. Initial data for all of these models are obtained from the relativistic, rotating star equilibrium code of [47]. Stars A and B were also studied in Paper I [49]. For the differentially rotating stars C, D, and E, we choose the initial rotation profile

$$u^t u_\varphi = R_{\text{eq}}^2 A^2 (\Omega_c - \Omega), \quad (69)$$

where Ω is the angular velocity of the fluid, Ω_c is the value of Ω at the center and all along the rotation axis, R_{eq} is the equatorial coordinate radius, and the parameter A , which measures the degree of differential rotation, is chosen to be unity. In the Newtonian limit, Eq. (69)

TABLE I: Initial equilibrium models for code tests.

Star	M	M_0	R_{eq}/M	$\rho_{0,\text{max}}^{\text{a}}$	$T/ W $	$\Omega_{\text{eq}}/\Omega_c^{\text{b}}$	$P_{\text{rot}}/M^{\text{c}}$	$\mathcal{R}_{\text{pe}}^{\text{d}}$
A	0.170	0.186	4.10	0.241	0.032	1.0	155	0.88
B	0.171	0.187	3.48	0.363	0.031	1.0	125	0.87
C	0.183	0.200	4.53	0.155	0.095	0.346	60.6	0.73
D	0.241	0.260	5.47	0.061	0.234	0.383	52.4	0.37
E	0.259	0.277	5.92	0.045	0.263	0.381	57.4	0.28

^a Maximum rest-mass density. This does not correspond to the center of the star for hypermassive, toroidal models D and E.

^b Ratio of Ω at the equatorial surface to Ω at the center.

^c Initial central rotation period.

^d Ratio of polar to equatorial coordinate radius.

reduces to the so-called “ j -constant” law [50]

$$\Omega = \frac{\Omega_c}{1 + \frac{\varpi^2}{R_{\text{eq}}^2 A^2}}. \quad (70)$$

We note that the maximum mass, $n = 1$ TOV polytrope has mass $M = 0.164$ and compaction $R_{\text{eq}}/M = 3.59$ [47]. All of the axisymmetric tests in this section were performed with a modest resolution of 64×64 and outer boundaries at about $12M$. Passing these tests successfully with modest resolution helps establish the robustness of our code.

A. Tests in axisymmetry

To demonstrate that our “axisymmetrized” code can distinguish stable and unstable uniformly rotating models, we consider stars A and B. These stars lie along a sequence of constant angular momentum, uniformly rotating stars. As described in Paper I, star A lies to the left of the turning point on the M - ρ_c equilibrium curve, while star B lies to the right. Then by the theorem of Friedman, Ipser, and Sorkin [51], star B is secularly unstable to radial perturbations, while star A is stable. Since the onset of dynamical radial instability is very close to the onset of secular instability for such sequences [20], we expect that star A will be stable to collapse, while star B will be dynamically unstable. When evolved in axisymmetry, star A persists for more than $7P_{\text{rot}}$ without significant changes in structure, where the central rotation period is

$$P_{\text{rot}} \equiv \frac{2\pi}{\Omega_c(t=0)}. \quad (71)$$

The oscillations in ρ_c , which correspond to radial pulsations, have an amplitude of $\lesssim 7\%$. For this run, the Hamiltonian and momentum constraints are satisfied to within 2%, while M is conserved to better than 1%. Meanwhile, the unstable uniformly rotating star (star B) collapses, with an apparent horizon first appearing at time $t \simeq 2P_{\text{rot}}$, corresponding to 21.3 light crossing

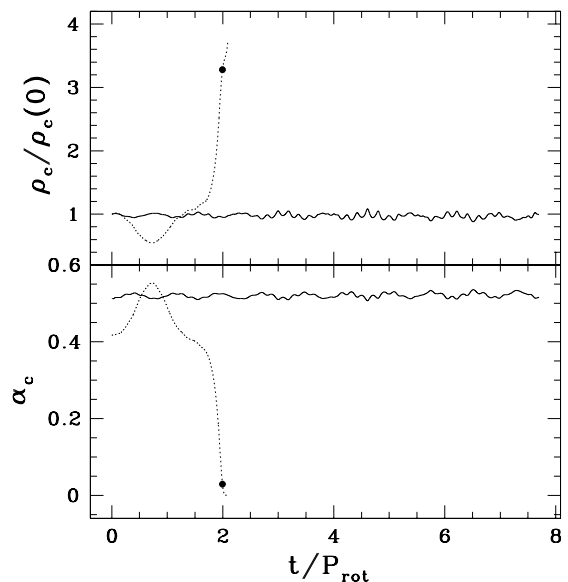


FIG. 1: Axisymmetric evolution of uniformly rotating stars. Star A (solid lines) is stable, while star B (dotted lines) is unstable to collapse. The upper window shows the central density normalized to its initial value, while the lower gives the central lapse. The solid dot indicates the first appearance of an apparent horizon during the collapse of star B.

times of the grid. At this time, the constraints are satisfied to within 6% and M is conserved to within 3%. Thus, stable and unstable uniformly rotating stars are clearly distinguished even at this moderate resolution. Figure 1 summarizes the results for these two runs.

Next we consider the evolution of a differentially rotating star using our axisymmetric code. We evolve star C for a time $\gtrsim 15P_{\text{rot}}$. Throughout the simulation, all constraints are satisfied to better than 4.5%, while M , J , and M_0 are conserved to within 3.5% (J and M_0 decrease due

to flow beyond the outer boundaries). In the absence of a dissipative mechanism to brake the differential rotation, the structure of the equilibrium star should not change. We find that we can numerically hold this equilibrium state for $15P_{\text{rot}}$. Note that the small amount of Kreiss-Oliger dissipation employed for numerical stability does not alter the rotation profile of the star. After this time, inaccuracies at the center, manifested by growth in Ω and high-frequency oscillations in ρ_0 , begin to grow. We monitor the evolution of the circulation for three different fluid elements chosen at the following initial locations in the equatorial plane: (a) $r = R_{\text{eq}}/4$, (b) $r = R_{\text{eq}}/2$, and (c) $r = 3R_{\text{eq}}/4$, where R_{eq} is the initial radius of the star. We find that, for $t \lesssim 22.5P_{\text{rot}}$, the circulation is conserved to better than 5% for all three of these points. After this time, the same inaccuracies cause the circulation to deviate from its initial value.

Because viscosity tends to smooth irregularities in the velocity field, the problems near the axis and the inaccuracy of the azimuthal velocity can be controlled by a small shear viscosity. To test this we evolve star C for $\sim 60P_{\text{rot}}$ with a very small shear viscosity (such that $\tau_{\text{vis}} \simeq 550P_{\text{rot}}$). Because τ_{vis} is so much greater than the length of the simulation, the small viscosity does not significantly alter the structure of the star. We find that the behavior of Ω improves considerably, while the small-scale variations in ρ_0 near the axis do not occur. In addition, the circulation values for the same three points which we studied in the previous case are conserved to within 5% for more than $50P_{\text{rot}}$. Thus, even a tiny shear viscosity significantly lengthens the period during which our runs are accurate. As we will describe below, the presence of a small shear viscosity allows us to evolve axisymmetric models accurately for hundreds of P_{rot} , corresponding to thousands of M .

B. Tests of dynamical bar mode sensitivity

We now demonstrate that our 3D code is sensitive to the nonaxisymmetric *dynamical* bar-mode instability. This sensitivity is important because the results of axisymmetric runs for a particular case will only be valid physically if it can be demonstrated that nonaxisymmetric modes do not develop in the corresponding 3D evolution. We consider two models, D and E, which we expect to be dynamically stable and unstable to bars, respectively. This expectation is based on earlier 3+1 fully relativistic evolutions of these stars by Shibata, Baumgarte, and Shapiro [52], who studied the formation of bars. Both models are hypermassive, toroidal configurations with high values of $T/|W|$ (0.230 for D and 0.258 for E). These models are identical to models D1 and D2 considered in [52]. To test for bars, we add a nonaxisymmetric density perturbation of the following form to the

axisymmetric initial data:

$$\rho = \rho_0 \left(1 + \delta_b \frac{x^2 - y^2}{R_{\text{eq}}^2} \right), \quad (72)$$

where δ_b parameterizes the strength of the initial bar deformation. We choose $\delta_b = 0.1$ for both models D and E. We then re-solve the constraint equations as in [53] to ensure that they are satisfied on the initial time slice. The growth of a bar is indicated by the quadrupole diagnostic (see [54]),

$$Q = \langle e^{im\varphi} \rangle_{m=2} = \frac{1}{M_0} \int d^3x \rho_* \frac{(x^2 - y^2) + 2ixy}{x^2 + y^2}. \quad (73)$$

We will take $|Q| = \sqrt{Q^*Q}$ as a measure of the magnitude of the bar deformation.

We evolve star D for a time $8.9P_{\text{rot}}$, during which M and J were conserved to within 0.7% and all constraints were satisfied to within 2%. For Star E, the run was terminated after $6.3P_{\text{rot}}$ and M and J were conserved to within 1.0%, while constraint violations were $\lesssim 5.5\%$. Both runs were performed in π -symmetry on uniform grids with resolution $128 \times 64 \times 32$. The outer boundaries in the x - y plane were at $16.6M$ for star D and $19.3M$ for star E. The results are shown in Fig. 2. This test clearly shows the growth of the bar mode for star E, while star D does not form a bar even with the substantial initial perturbation.

C. Tests with viscosity

As a first test of our shear viscosity implementation, we demonstrate that uniformly rotating configurations are unaffected by the presence of even a large viscosity. We evolve the uniformly rotating, stable star A with $\nu_P = 0.2$ (such that $\tau_{\text{vis}} \simeq 0.09P_{\text{rot}}$) for $\sim 100P_{\text{rot}} \sim 15,500M$. The mass M is conserved to within 0.1%, and J to within 1.5%. (Note that, even in axisymmetry, J is not identically conserved by our finite differencing scheme when viscosity is present.) All constraints are satisfied to better than 1.1% for the duration of this run. The resulting evolution of the central rest-mass density and central angular velocity are shown in Fig. 3. These quantities oscillate on the radial oscillation timescale ($\sim \tau_{\text{FF}}$) with amplitudes of several percent, and this run encompassed roughly 120 oscillation periods. Because the oscillations are radial, they are not appreciably damped by the shear viscosity. For the entire run, the average values of ρ_c and Ω_c drop by about 4.5% and 6.5%, respectively. These small deviations are due to the accumulated numerical error of the finite differencing and are reduced by increasing resolution. Since the star does not change appreciably over many viscous timescales, our code simulates the correct physical behavior for this case.

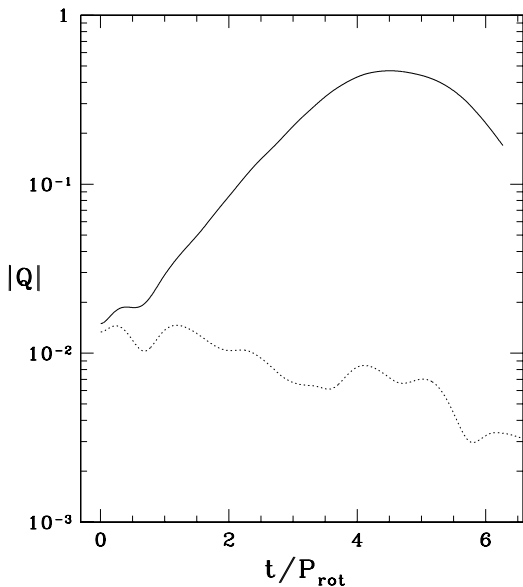


FIG. 2: Quadrupole diagnostic for evolutions of rapidly rotating hypermassive stars. Star D is stable and star E is unstable to dynamical bar formation. The initial $m = 2$ perturbation decays for star D (dotted line) but grows for star E (solid line). Note that, for each curve, the time axis is normalized by P_{rot} which differs for the two stars.

We now test the viscous evolution of the differentially rotating star C. We choose viscosity $\nu_P = 0.015$, so that Eq. (43) gives $\tau_{\text{vis}} \approx 5.5P_{\text{rot}}$. In axisymmetry, we ran this case for $84.5P_{\text{rot}} = 15.4\tau_{\text{vis}} = 5,120M$, during which time M and J are conserved to within 0.4% while all of the constraints are satisfied to better than 1.1%. Figure 4 shows several snapshots of the angular velocity profile in the equatorial plane for the 2D case taken at various times. This clearly shows that the presence of viscosity drives the star toward uniform rotation. As a quantitative test of the action of viscosity, we check that the circulation evolves according to Eq. (66). Choosing three fluid elements in the initial configuration, we track these fluid elements and calculate the circulation \mathcal{C} for each one, as well as the time-integrated contributions from viscosity \mathcal{C}_{vis} [see Eq. (67)]. The fluid elements are chosen at the same locations as for the inviscid test of star C in Section III A. The results are shown in Fig. 5, which gives the circulation, the viscous contribution, and their sum, \mathcal{C}_{tot} . For all three cases, \mathcal{C}_{tot} is conserved to better than 2% for the entire run. Thus, angular momentum is transported correctly for many tens of rotation periods (thousands of M) when a significant shear viscosity is present.

We also used this case to test the scaling behavior of

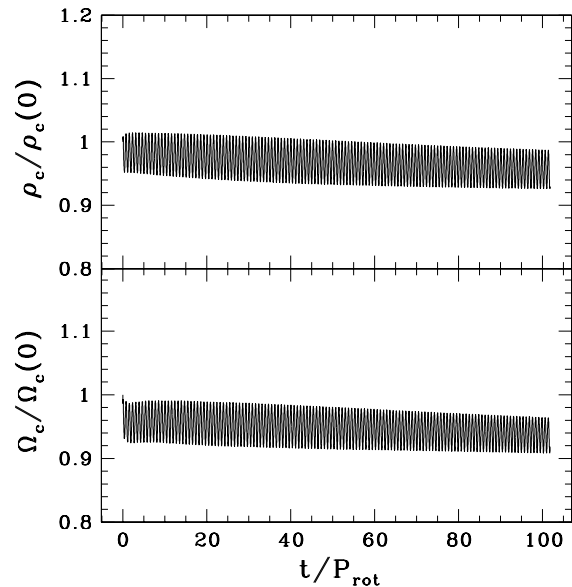


FIG. 3: Evolution of the stable, uniformly rotating star A with high viscosity. The central density (shown in the upper window) and central angular velocity (lower window) oscillate without changing appreciably for over 100 rotation periods ($15,500M$).

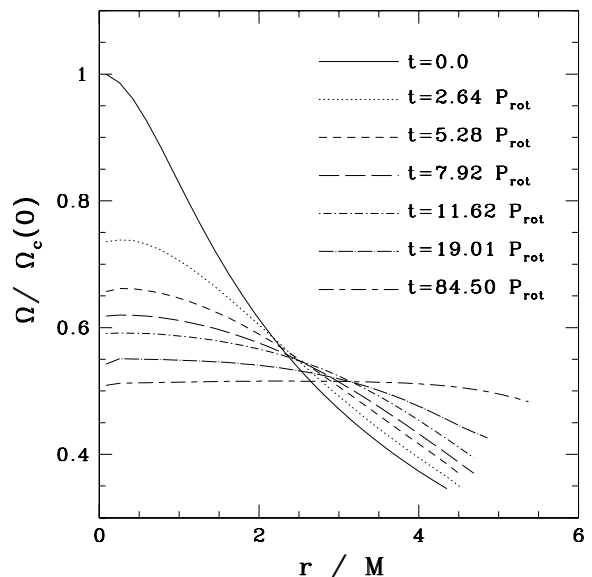


FIG. 4: Angular velocity profiles in the equatorial frame at selected times for star C with $\tau_{\text{vis}} \approx 5.5P_{\text{rot}}$. The presence of viscosity drives the star to uniform rotation on a viscous timescale.

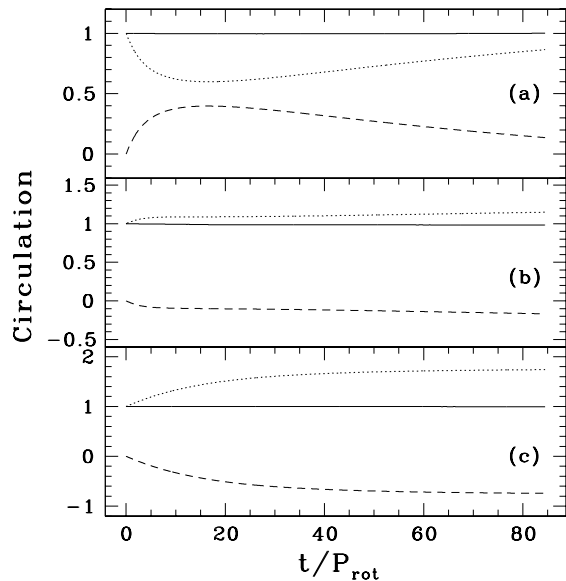


FIG. 5: Evolution of the circulation for three selected fluid elements of star C in axisymmetry (using $\nu_P = 0.015$). The dotted line gives the circulation \mathcal{C} , the dashed line gives the time integrated contribution due to viscosity \mathcal{C}_{vis} , and the solid line gives their sum \mathcal{C} , which is well-conserved [see Eq.(67)]. Each quantity is normalized by the corresponding initial circulation.

our solutions with ν_P . Results are shown in the upper window of Fig. 6, which gives the evolution of $\langle \sigma^{\mu\nu} \sigma_{\mu\nu} \rangle$ for several values of ν_P versus scaled time. We define the energy dissipation rate via shear viscosity, $\langle \sigma^{\mu\nu} \sigma_{\mu\nu} \rangle$, as in Section II E [see Eq. (16)]. This quantity decays due to the action of viscosity. The figure shows that our solutions obey the proper scaling with ν_P , i.e. they evolve identically but on a timescale inversely proportional to the adopted viscosity (ν_P). Hence our results can all be scaled to the much smaller viscosities likely to be appropriate for physically realistic viscosity in stars. We provide further demonstration of scaling in Section IV B 2 (see Fig. 13).

The results of the axisymmetric run with $\nu_P = \nu_0$ agree fairly well with a 3D, π -symmetric run performed for the same model. This 3D run employed $64 \times 32 \times 32$ grid zones, giving only half of the resolution of the axisymmetric run. We terminated the 3D run after $6.35 P_{\text{rot}}$. M is conserved to within 0.4%, while the constraint violations are $\lesssim 3.6\%$. Because of the lower resolution in this case, 3.2% of the total angular momentum is lost (as opposed to 0.4% for the much longer axisymmetric run). A comparison of $\langle \sigma^{\mu\nu} \sigma_{\mu\nu} \rangle$ for the 2D and 3D cases is plotted in the lower window of Fig. 6, and shows good agreement.

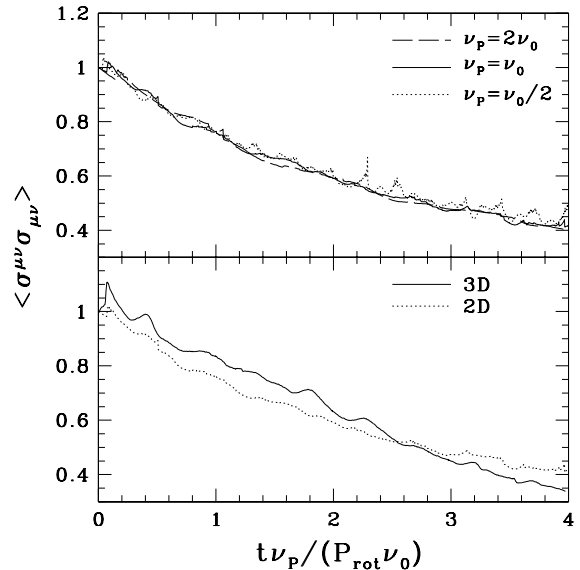


FIG. 6: Energy dissipation rate $\langle \sigma^{\mu\nu} \sigma_{\mu\nu} \rangle$, normalized to its initial value, for several runs with star C. The upper window demonstrates the proper scaling of our solutions with ν_P . Note that the time axis is scaled according to the appropriate value of ν_P . The lower window compares $\langle \sigma^{\mu\nu} \sigma_{\mu\nu} \rangle$ for runs in axisymmetry (2D) and π -symmetry (3D), both with $\nu_P = 0.015 = \nu_0$. These evolutions agree fairly well.

IV. DYNAMICAL EVOLUTIONS

A. Introduction and discussion of models

Having shown simulations for several test models, we now present the evolution of five differentially rotating, dynamically stable stellar models in which viscosity changes the structure of the stars in nontrivial ways. Our models are summarized in Table II and Fig. 7. We first perform short, 3D simulations without viscosity on all the five models to make sure that they are all dynamically stable to bar formation. Each of them is then evolved with our axisymmetric code in both the rapid and no-cooling limits described in Section II F. The initial data for the five stars are again computed with the relativistic equilibrium code of [47]. The stars obey an $n = 1$ polytropic equation of state $P = \rho_0^2$. We adopt the rotation law given by Eq. (69) with $A = 1$. This rotation law has been found to be a good approximation to the angular velocity profile of proto-neutron stars formed from core collapse [55]. In the case of a binary neutron star merger, the remnant can form a dynamically stable hypermassive neutron star provided the remnant mass does not exceed about 1.7 times the maximum mass of a nonrotating spherical star [10]. Our adopted rotation law is also found to be a reasonably good approximation to the angular velocity profile of these hypermassive

TABLE II: Initial Models

Case	$M_0/M_{0,\text{TOV}}^{\text{a}}$	$M_0/M_{0,\text{sup}}^{\text{b}}$	M	R_{eq}/M	J/M^2	$T/ W $	$\Omega_{\text{eq}}/\Omega_c$	P_{rot}/M	ν_P^{c}
I	1.69	1.38	0.279	4.48	1.0	0.249	0.33	38.4	0.2
II	1.39	1.13	0.228	4.40	0.85	0.188	0.32	41.3	0.07
III	1.39	1.13	0.232	5.54	1.0	0.224	0.37	54.2	0.15
IV	1.39	1.13	0.234	6.27	1.1	0.244	0.31	63.3	0.2
V	1.0	0.81	0.168	8.12	1.0	0.181	0.40	103	0.15

^a If this ratio is greater than unity, the star’s mass exceeds the TOV limit for $n = 1$ polytropes ($M_{0,\text{TOV}} = 0.180$).

^b If this ratio is greater than unity, the star’s mass exceeds the uniformly rotating (supramassive) upper limit ($M_{0,\text{sup}} = 0.221$) and is therefore hypermassive.

^c The values of ν_P are chosen such that the viscous timescale $\tau_{\text{vis}} \approx 3P_{\text{rot}} \sim 10\tau_{\text{FF}}$.

neutron stars [8].

In all of our axisymmetric calculations, we use a grid size 128×128 with an outer boundary at $14M$ for the most massive and compact star (star I), and $24M$ for the least massive and compact star (star V). Initially, the equatorial radii of the stars are only about $R_{\text{eq}} \approx 5M$. However, viscosity causes the outer layers to expand and, in some cases, we find that a few percent of rest mass is lost due to material flowing out of the grid. In each model, we choose the value of the viscosity coefficient ν_P such that the viscous timescale defined by Eq. (43) is $\tau_{\text{vis}} \approx 3P_{\text{rot}} \sim 10\tau_{\text{FF}}$. With this moderate strength of viscosity, we need to evolve the stars for 100 – $200P_{\text{rot}}$ in most cases to follow the complete secular evolution and determine the final fate of the stars. The reason is that in most cases, viscosity generates a low-density envelope around the central core. Since our viscosity law has $\eta \propto P$, the viscosity in the low-density region is small. (The density throughout the envelope is greater, however, than the cutoff density below which $\eta = 0$.) Hence the effective viscous timescale increases with time and it takes longer for the stars to achieve a final state.

Four of the five stars we consider are hypermassive, and we expect viscosity to change their structure significantly. Star I is the most hypermassive star ($M_0 = 1.38M_{0,\text{sup}}$, where $M_{0,\text{sup}} = 0.221$ is the mass limit for uniformly rotating $n = 1$ polytropes, i.e. for stars at the mass-shedding limit [47]). We find that this star eventually collapses to a black hole, but a substantial amount of rest mass is leftover to form a massive accretion disk. We consider three other hypermassive models (stars II, III and IV) to study whether or not all hypermassive neutron stars will collapse in the presence of viscosity. Stars II, III and IV have the same rest mass ($M_0 = 1.13M_{0,\text{sup}}$) which is slightly smaller than that of star I but different angular momenta J . We find that stars III and IV never collapse, but evolve in a quasi-stationary manner to a uniformly rotating core surrounded by a low-density, disk-like envelope. Star II eventually collapses to a black hole if we impose rapid cooling. In the no-cooling limit, however, this model forms a uniformly rotating core sur-

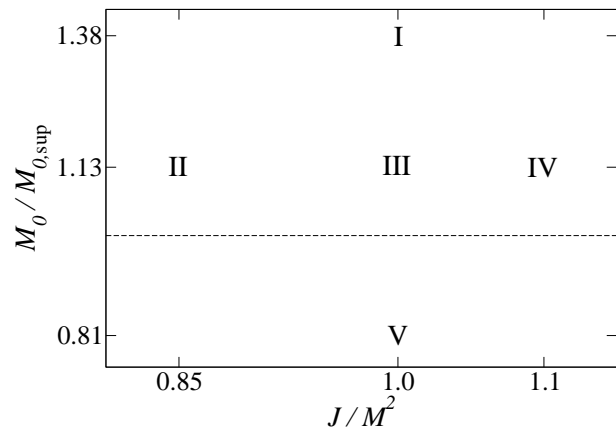


FIG. 7: Rest mass M_0 and spin parameter J/M^2 for the five selected models in Table II. The dashed line denotes the mass limit of uniformly rotating supramassive $n = 1$ polytropes, $M_0 = M_{0,\text{sup}}$. All stars above this line are hypermassive and require differential rotation to be in hydrostatic equilibrium.

rounded by a substantial disk. Star V is the only non-hypermassive model. As expected, this star does not collapse under the action of viscosity. However, viscosity cannot drive the whole star to rigid rotation, because the angular momentum of the star exceeds the maximum angular momentum allowable for a rigidly-rotating star having the same rest mass. Instead, viscosity again leads to a uniformly rotating core and a differentially rotating disk-like envelope. The final outcomes of the five models are summarized in Table III.

We also performed 3D simulations on stars I and IV to search for unstable, nonaxisymmetric secular modes. A nonaxisymmetric bar instability usually develops when a star is rotating rapidly, i.e. has a sufficiently large $T/|W|$. Of the five models we study, stars I and IV have the highest $T/|W|$. We do not find any nonaxisymmetric insta-

TABLE III: Summary of simulations.

Case	2D/3D	Cooling	$t_{\text{final}}/P_{\text{rot}}$ ^a	Initial $T/ W $	Final $T/ W $	$\langle P/\rho^\Gamma \rangle^b$	Fate	J_h/M_h^2 ^c	$M_{0,\text{disk}}/M_0$	J_{disk}/J
I	2D	no	28.9	0.25	0.09 ^d	3.9	BH + disk	0.6	0.23	0.65
	2D	yes	13.7		0.15 ^d	1.0	BH + disk	0.8	0.21	0.55
	3D	yes	9.3		0.21 ^d	1.0	BH + disk	0.8	0.18	0.47
II	2D	no	286	0.19	0.09	2.8	star + disk	–	0.15	0.56
	2D	yes	57.7		0.14 ^d	1.0	BH + disk	0.7	0.10	0.36
III	2D	no	105	0.22	0.09	4.3	star + disk	–	0.21	0.68
	2D	yes	315		0.12	1.0	star + disk	–	0.15	0.58
IV	2D	no	99	0.23	0.10	7.3	star + disk	–	0.25	0.76
	2D	yes	235		0.13	1.0	star + disk	–	0.17	0.62
	3D	yes	11.5		–	1.0	no bar	–	–	–
V	2D	no	105	0.18	0.09	3.7	star + disk	–	0.13	0.52
	2D	yes	171		0.13	1.0	star + disk	–	0.09	0.38

^a The time at which the simulation was terminated.

^b This quantity corresponds to an average of P/ρ^Γ over the final configuration of the star weighted by rest-mass density at the end of the simulation. Thermal pressure generated by viscous heating causes $P/\rho^\Gamma > 1$ (recall $\kappa = 1$). We find that the viscous heating is much more significant in the low-density region than in the core.

^c These values are obtained by solving Eqs. (74)–(82).

^d The quantity $T/|W|$ is undefined when the star undergoes a dynamical collapse. The number given here is an approximate value before the star becomes dynamically unstable.

bilities in these two models, and the 3D results roughly agree with the axisymmetric results.

We discuss the results of our simulations in detail in the following subsections.

B. Star I

1. 2D with no cooling

Star I is the most massive neutron star we study. We first perform an axisymmetric calculation with no cooling. At $t = 0$, the star has a toroidal density profile, i.e., the maximum density occurs off center (see the upper left panel of Fig. 9). As viscosity gradually brakes differential rotation, the star readjusts to a monotonic density profile. Figure 8 shows the maximum rest-mass density and the minimum value of the lapse as a function of time. Figure 9 shows the meridional rest-mass density contours at various times. We see that a meridional current is built up in the process. However, the magnitude of the meridional velocity ($\lesssim 0.01c$) is much smaller than the typical rotational velocity ($\sim 0.3c$).

Viscosity destroys differential rotation and transfers angular momentum to the outer layers. In the early phase of the evolution, the core contracts and the outer layers expand in a quasi-stationary manner. As the core becomes more and more rigidly-rotating, it approaches instability because the star is hypermassive and cannot support a massive rigidly-rotating core. At time $t \approx 27P_{\text{rot}} \approx 11\tau_{\text{vis}}$, the star becomes dynamically unstable and collapses. An apparent horizon appears at

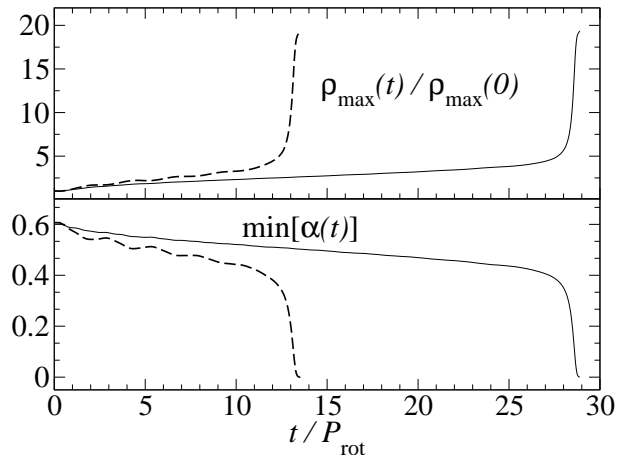


FIG. 8: Maximum value of rest-mass density (upper panel) and minimum value of lapse (lower panel) as a function of time for star I in the presence of viscosity. The solid (dashed) curves represent the case without (with) cooling. In both cases, the central core collapses to a black hole, and leaves behind a massive accretion disk.

time $t \approx 28.8P_{\text{rot}}$. Without black hole excision, the code crashes about $10M$ after the horizon appears because of grid stretching. About 30% of rest mass remains outside the apparent horizon at this point. We then continue the evolution using the excision technique described in [25]. We are able to extend the evolution reliably for

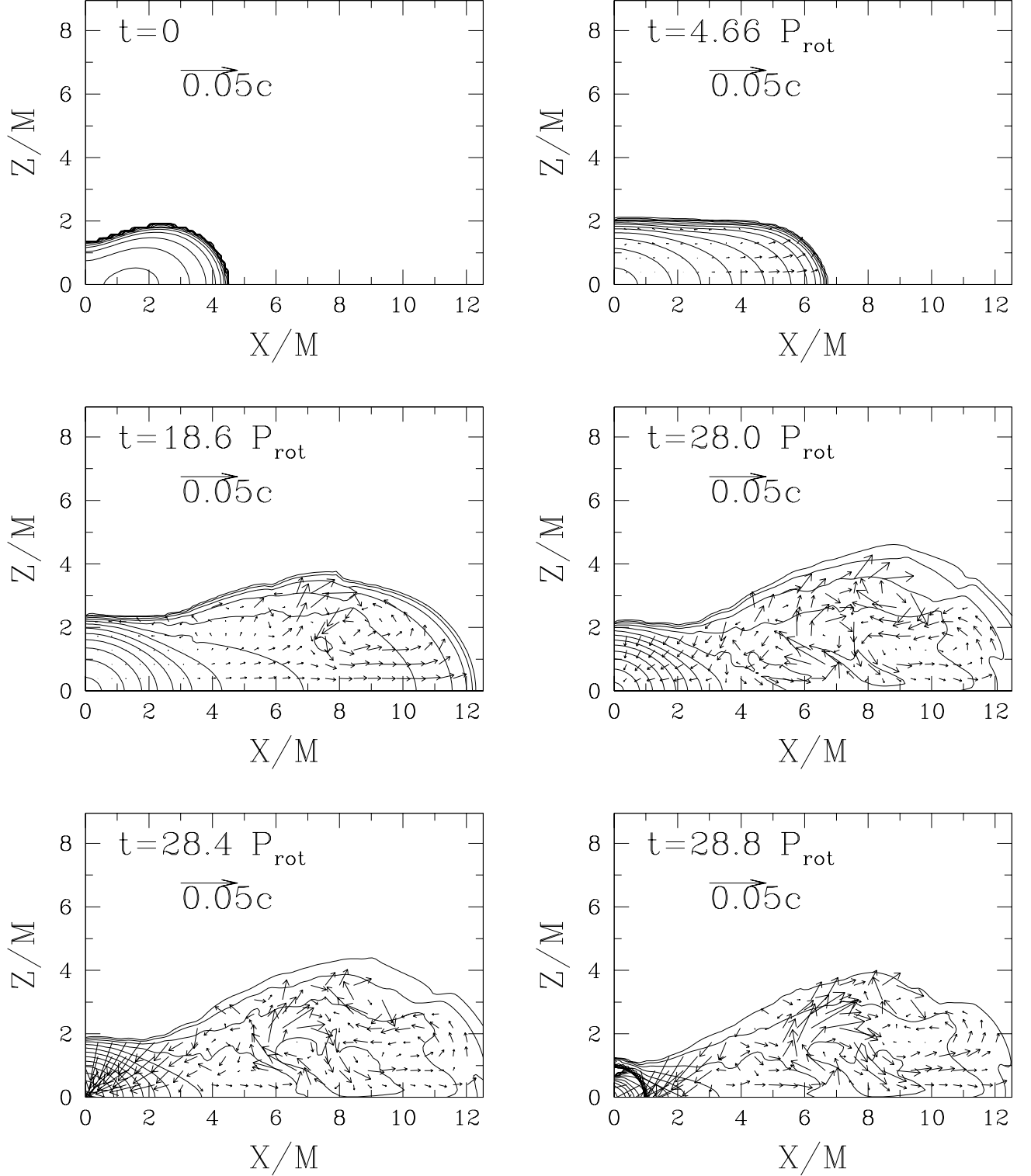


FIG. 9: Meridional rest-mass density contours and velocity field at various times for star I. The simulation was performed by assuming that the system is axisymmetric and experiences no cooling. The levels of the contours (from inward to outward) are $\rho_0/\rho_{0,\text{max}} = 10^{-0.15(2j+0.6)}$, where $j = 0, 1, \dots, 12$. In the lower right panel ($t = 28.8 P_{\text{rot}}$), the thick curve denotes the apparent horizon.

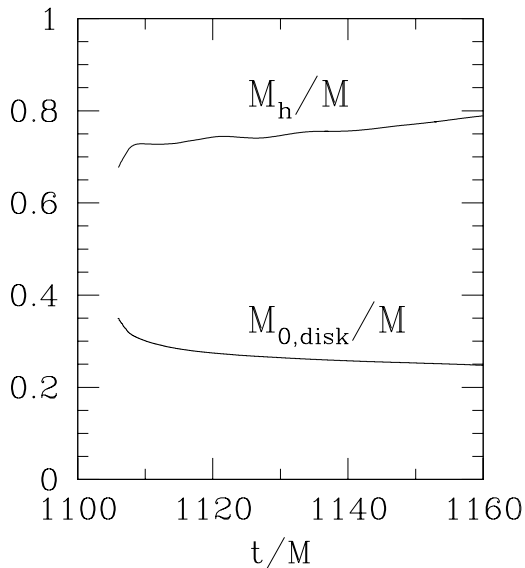


FIG. 10: Evolution of the black hole mass M_h and the rest mass of the disk $M_{0,\text{disk}}$ after the appearance of the apparent horizon at $t = 1106M = 28.8P_{\text{rot}}$. Note that time is plotted in units of M ($1P_{\text{rot}} = 38.4M$). Black hole excision is employed to track this late evolution.

another $55M$. The system settles down to a black hole surrounded by a massive ambient disk. The rest mass $M_{0,\text{disk}}$ and angular momentum J_{disk} of the disk can be calculated by integrating the rest-mass and angular momentum density over the volume outside the apparent horizon [c.f. Eqs. (57) and (51)]. The mass of the black hole can be estimated by the proper circumference of the horizon in the equatorial plane: $M_h = C_h/4\pi$ (assuming that the spacetime can be described by a Kerr metric). Figure 10 shows the evolution of M_h and the rest mass of the disk $M_{0,\text{disk}}$. We estimate the final values of M_h , $M_{0,\text{disk}}$, and J_{disk} by fitting these curves to analytic functions of the form $A + B \exp(-Ct)$ and extrapolating these fitting functions to $t \rightarrow \infty$ [56]. We estimate that the mass of the final black hole is $M_h \approx 0.82M$. The asymptotic rest mass and angular momentum of the ambient disk are found to be $M_{0,\text{disk}} \approx 0.23 M_0$ and $J_{\text{disk}} \approx 0.65J$. We can infer from the conservation of angular momentum that the final angular momentum of the black hole is $J_h \approx 0.35J$. Hence we find $J_h/M_h^2 \approx 0.52(J/M^2) \approx 0.52$.

The formation of a massive disk is mainly due to the fact that viscosity transports angular momentum from the inner core to the outer layers. The material in the outer region is unable to fall into the black hole because of the centrifugal barrier. The final mass of the black hole and disk can also be estimated independently from the conservation of specific angular momentum using a method developed by Shapiro and Shibata [57], which we apply below.

During the dynamical collapse, the effect of viscosity is negligible. Since the spacetime is axisymmetric, the

specific angular momentum $j = hu_\varphi$ of a fluid particle is conserved. For a Kerr black hole of mass M_h and angular momentum J_h , the specific angular momentum of a particle at the innermost stable circular orbit (ISCO) j_{ISCO} is given by

$$j_{\text{ISCO}} = \frac{\sqrt{M_h r_{\text{ms}}}(r_{\text{ms}}^2 - 2a\sqrt{M_h r_{\text{ms}}} + a^2)}{r_{\text{ms}}(r_{\text{ms}}^2 - 3M_h r_{\text{ms}} + 2a\sqrt{M_h r_{\text{ms}}})^{1/2}}, \quad (74)$$

where $a \equiv J_h/M_h$. The ISCO radius is

$$r_{\text{ms}} = M_h[3 + Z_2 - \sqrt{(3 - Z_1)(3 + Z_1 + 2Z_2)}], \quad (75)$$

where

$$Z_1 = 1 + \left(1 - \frac{J_h^2}{M_h^4}\right)^{1/3} \left[\left(1 + \frac{J_h}{M_h^2}\right)^{1/3} + \left(1 - \frac{J_h}{M_h^2}\right)^{1/3} \right] \quad (76)$$

and

$$Z_2 = \left(3 \frac{J_h^2}{M_h^4} + Z_1^2\right)^{1/2}. \quad (77)$$

The rest mass and angular momentum of the escaping matter in the envelope with $j > j_{\text{ISCO}}$ is given by

$$M_{0,\text{disk}} = \int_{j > j_{\text{ISCO}}} \rho_* d^3x, \quad (78)$$

$$J_{\text{disk}} = \int_{j > j_{\text{ISCO}}} \rho_* j d^3x. \quad (79)$$

We assume that the energy radiated by gravitational waves is negligible so that the total mass-energy of the system is approximately conserved. Hence we have

$$M = M_h + M_{\text{disk}}, \quad (80)$$

$$J = J_h + J_{\text{disk}}. \quad (81)$$

For a bound system, the contribution to the mass-energy of the matter in the disk, M_{disk} , is smaller than its rest mass $M_{0,\text{disk}}$. We write

$$M_{\text{disk}} = qM_{0,\text{disk}}. \quad (82)$$

We consider two opposite limits for q : $q = 1$ and $q = M/M_0$. The value $q \approx 1$ is a good approximation in the weak gravity regime. In the limit where $M_h \ll M$, we have $M_{\text{disk}} \approx M$ and $M_{0,\text{disk}} \approx M_0$. Hence in this limit, $q \approx M/M_0$, which is 0.92 for star I (see Table II). We expect that the correct q lies somewhere between these two extremes, which are not very different. The mass and angular momentum of the black hole can be estimated by solving the system of transcendental Eqs. (74)–(82) at a particular time slice during the pre-excision dynamical collapse phase, including the time slice at the onset of dynamical collapse (where q is close to unity). We find that the values of M_h and J_h are insensitive to q . They are also insensitive to which time slice we choose to do the calculation. We find $M_h \approx 0.75M$ and

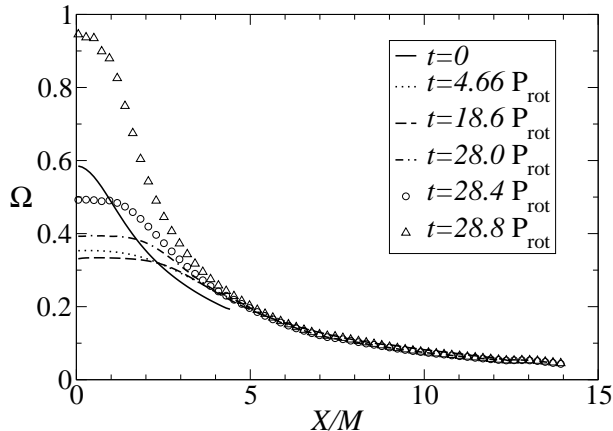


FIG. 11: Angular velocity profiles in the equatorial plane at various times during the evolution of star I.

$J_h \approx 0.35J$ ($J_h/M_h^2 \approx 0.6$). The rest mass in the ambient disk is found to be $M_{0,\text{disk}} \approx 0.23M_0$. It should be noted that this calculation is based on the assumptions that the spacetime around the disk can be approximated by a Kerr metric, and that the disk is moderately thin and lies in the equatorial plane of the hole. This approximation is not reliable when the disk is massive ($M_{\text{disk}} \approx M$). In our case, we find this calculation agrees rather well with the actual asymptotic values determined by the dynamical simulation with excision. Henceforth we will use Eqs. (74)–(82) to estimate M_h , J_h , $M_{0,\text{disk}}$ and J_{disk} whenever an apparent horizon forms.

Since viscosity is small in the low-density region, it takes longer to remove the differential rotation in the outer layers. Figure 11 shows the angular velocity profiles at various times. We see that by the time the inner core collapses, the material in the outer layers is still differentially rotating. After the dynamical collapse, viscosity will cause some of the remaining material to slowly accrete onto the black hole.

We monitor the conserved quantities and the constraints during the entire evolution. Since our finite-difference scheme preserves the rest mass, the variation of M_0 can only come from material flowing out of the grid. We find that M_0 is conserved to 0.01%, and angular momentum is conserved to 0.1%. The Hamiltonian constraint is violated by less than 0.3% before the dynamical collapse occurs. It increases to 3% by the time an apparent horizon appears. The momentum constraints are violated by less than 1% before the dynamical collapse occurs, and increase to 6% by the time an apparent horizon appears.

We next perform an axisymmetric simulation of star I with rapid cooling. The dashed lines in Fig. 8 show the time evolution of the maximum rest-mass density and the minimum value of the lapse. As in the no-cooling case, the inner core contracts and the outer layers expand in a quasi-stationary manner. The core then collapses dynamically to a black hole and leaves behind a massive accretion disk. Since there is no viscous heating, the whole process occurs more quickly than in the no-cooling case. The dynamical collapse occurs at time $t \approx 12P_{\text{rot}} \approx 5\tau_{\text{vis}}$ and the apparent horizon appears at $t \approx 13.5P_{\text{rot}}$. Figure 12 shows the meridional rest-mass density contours at various times. We estimate, by solving Eqs. (74)–(82) at $t \approx 13.5P_{\text{rot}}$ with $q = 1$, that the mass and angular momentum of the final black hole are $M_h \approx 0.75M$ and $J_h \approx 0.45J$ ($J_h/M_h^2 \approx 0.8$). About 20% of rest mass escapes capture to form an accretion disk.

In Section III C, we demonstrated that when the viscous timescale is significantly longer than the dynamical timescale, the secular rates of change of all physical quantities scale inversely with viscosity. The secular evolution of star I with rapid cooling is short enough for us to perform another detailed scaling test. Figure 13 demonstrates this scaling behavior by evolving star I with four different strengths of viscosity $\nu_P = 0.4, 0.2, 0.1$, and 0.05 . (The curves in Fig. 8 correspond to $\nu_P = 0.2$.) We see that the scaling holds until dynamical collapse at time $t \approx t_d(\nu_P)$. When $t \gtrsim t_d$, the evolution of the system is no longer driven by viscosity. We therefore expect that the collapse is independent of the strength of viscosity as long as the viscous timescale is much longer than the dynamical timescale. In the lower panel of Fig. 13, we demonstrate that it is possible to shift the time axes ($t \rightarrow t - t_d$) so that the four viscosity runs yield the same result when $t - t_d \gtrsim 0$, which indicates that viscosity is insignificant during the dynamical collapse. The values of t_d are determined by requiring that the scaling relation $t_d(\nu_2)/t_d(\nu_1) \approx \nu_1/\nu_2$ holds, and that the four curves be aligned when plotted against the shifted time $t - t_d(\nu_P)$. We found that $t_d(\nu_P)/P_{\text{rot}} \approx 6.1, 12.0, 24.08$ and 47.75 respectively for $\nu_P = 0.4, 0.2, 0.1$, and 0.05 . The fact that we are able to find $t_d(\nu_P)$ that satisfies these requirements validates our physical interpretation of the two phases of evolution.

To better visualize the effects of viscosity, we follow the motions of ten selected Lagrangian fluid elements. Figure 14 shows the worldlines of these particles. We choose the particles to be in the equatorial plane of the star. Equatorial symmetry implies that the particles will remain in the equatorial plane at all times. The position of a fluid particle X satisfies the equations

$$\frac{d}{dt}X(t) = \frac{u^x(t; X(t))}{u^t(t; X(t))}. \quad (83)$$

We label the particles by the initial fraction of rest mass interior to the cylinder of radius X . We see that the

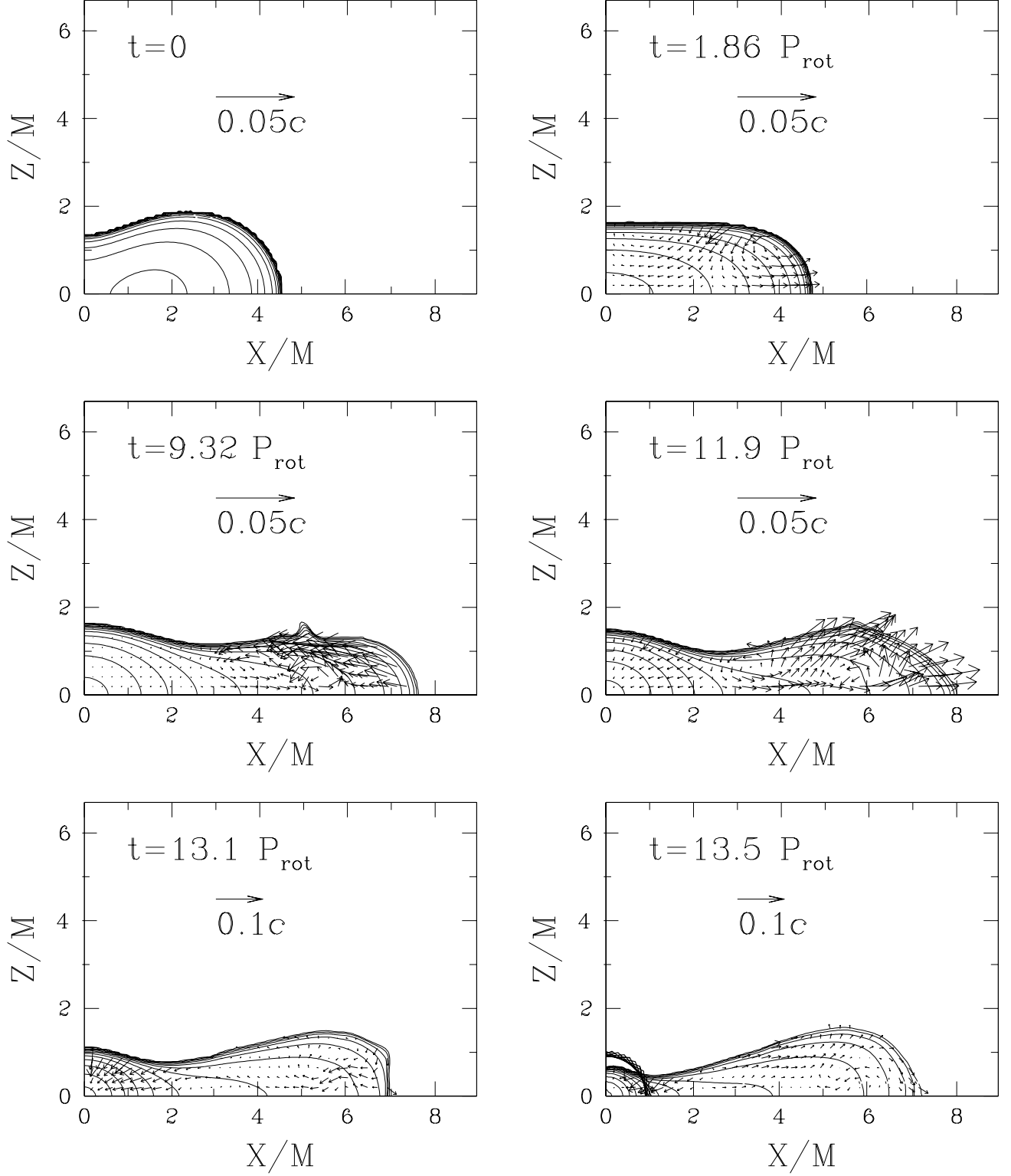


FIG. 12: Same as Fig. 9 but for rapid cooling.

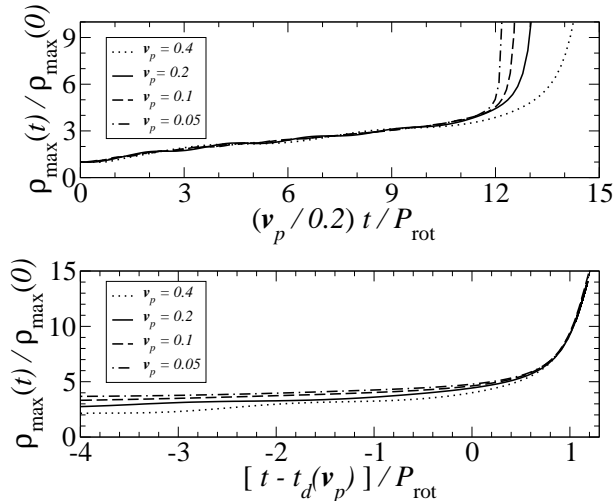


FIG. 13: Evolution of the maximum rest-mass density of star I for various strengths of viscosity, assuming rapid cooling. Upper panel: the curves coincide when plotted against the scaled time prior to dynamical collapse. Lower panel: during dynamical collapse, it is possible to shift the time axes $[t \rightarrow t - t_d(\nu_p)]$ so that the curves again coincide, which indicates that viscosity plays an insignificant role during the dynamical collapse phase.

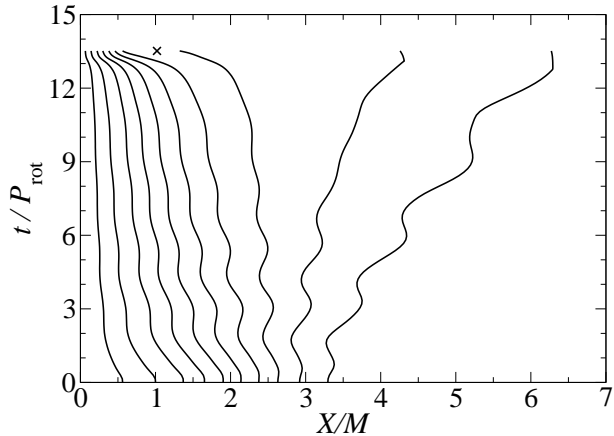


FIG. 14: The worldlines of Lagrangian fluid elements at the equator for star I, assuming rapid cooling. The cylindrical coordinate X of the particles at time $t = 0$ is chosen so that the initial fraction of rest mass $m(X)$ interior to the cylinder of radius X is, from left to right, $m=0.03, 0.1, 0.2, 0.3, 0.4, 0.5, 0.6, 0.7, 0.8$ and 0.9 . The cross in the diagram denotes the location of the apparent horizon at the end of the simulation.

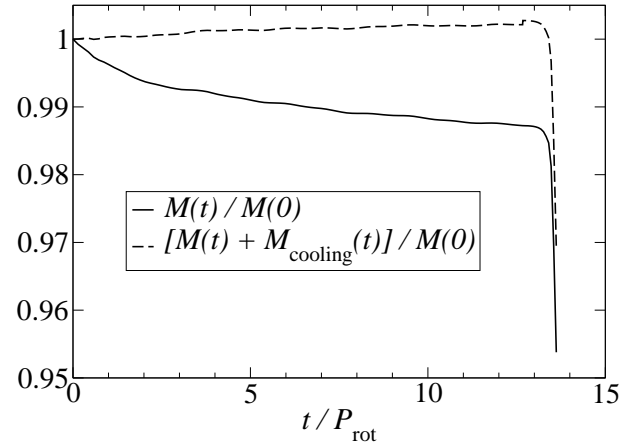


FIG. 15: Evolution of the mass M of star I in the rapid-cooling limit. The mass is not conserved since the thermal energy generated by viscous heating is removed. However, the sum of the remaining mass and the mass carried away by “radiation”, M_{cooling} , is approximated conserved.

particles with the initial mass fraction $m \lesssim m_* \simeq 0.8$ move toward the center and ultimately move inside the apparent horizon, while those with $m \gtrsim m_*$ move away from the center and remain outside the apparent horizon. This agrees with our estimates of the rest mass of the ambient disk.

Since there is rapid cooling, the mass is not conserved because the thermal energy generated by viscous heating is removed, as discussed in Section IIH. However, when we account for the mass-energy carried away by thermal radiation, M_{cooling} , the total mass $M_{\text{tot}} = M + M_{\text{cooling}}$ should be conserved approximately [see Eq. (56)]. Figure 15 shows M and M_{tot} as a function of time before an apparent horizon appears. The total mass is well-conserved except near the end of the simulation, where the numerical error arising from the grid stretching causes a few percent drop in the mass.

We monitored the violations of the constraints during the evolution. The violation of the Hamiltonian constraint is $\sim 0.1\%$ before the dynamical collapse occurs, and goes up to 7% at the time when the apparent horizon appears. The violations of the momentum constraints are also $\sim 0.1\%$ before the dynamical collapse occurs, and increase to 8% at the time when the apparent horizon appears.

C. Other models

The evolution of star II due to viscosity is different from that of star I. Although it is still hypermassive, the mass of star II is smaller than that of star I. When evolved

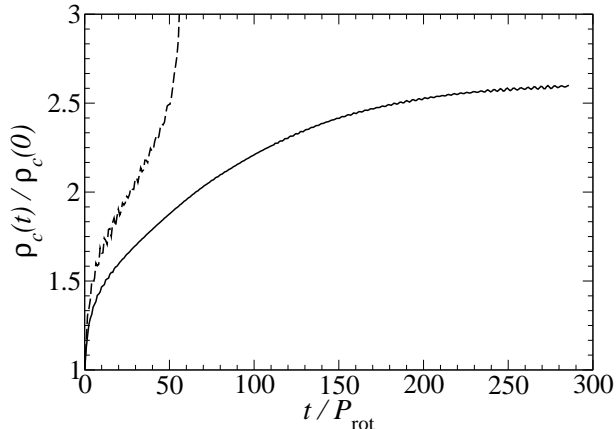


FIG. 16: Evolution of the central rest-mass density for star II with no cooling (solid line) and with rapid cooling (dashed line).

in the absence of cooling, the star does not collapse to a black hole, but forms a rigidly-rotating core with a low-density disk-like envelope. When evolved in the rapid-cooling limit, however, the star collapses to a black hole. Figure 16 shows the evolution of the central density.

In the no-cooling case, Star II has not collapsed to a black hole by the end of simulation ($t = 286P_{\text{rot}} = 87\tau_{\text{vis}} = 11,800M$), but is settling to a uniformly rotating core surrounded by a massive torus. Figure 17 shows the meridional density contours at the beginning and at the end of the simulation. Figure 18 shows the angular velocity profiles at various times. Viscosity drives the star to a quasi-equilibrium, rigidly-rotating core surrounded by a low-density disk. We cannot exclude the possibility that some of the outer material will slowly accrete onto the uniformly rotating inner core, eventually triggering collapse to a black hole. However the star acquires enhanced pressure support against collapse from viscous heating (i.e. $P/\rho_0^{\Gamma} > \kappa(0)$ where $\kappa(0) = 1$). Hence it may no longer be hypermassive with respect to this new “hot” equation of state, as the simulation suggests. During the entire simulation, the star loses 1.2% of its rest mass and 4.5% of its angular momentum due to material flowing out of the grid. Figure 19 shows the L2 norms of the Hamiltonian and momentum constraints defined by Eqs. (59) and (60) of Paper I. We see that the violation of all the constraints are smaller than 1% during the entire evolution of $286P_{\text{rot}} = 11800 M$.

The values of the ratio of kinetic to gravitational potential energy, $T/|W|$, for all of the stars we studied decrease with time. Figure 20 shows the evolution of $T/|W|$ for star II evolved without cooling. Viscosity transforms part of the rotational kinetic energy into heat. It also

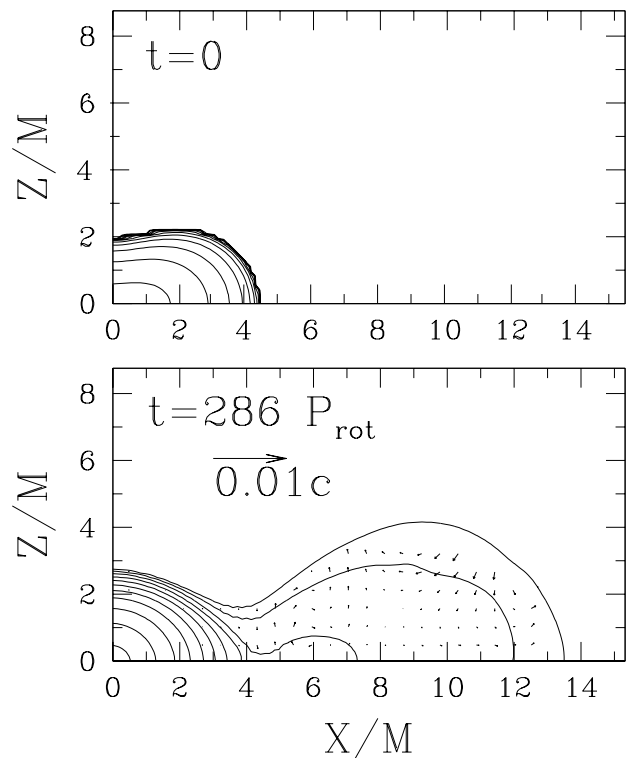


FIG. 17: Meridional rest-mass density contours for star II with no cooling. The upper graph shows the contours at $t = 0$ and the lower graph shows the contours at the end of the simulation ($t = 286P_{\text{rot}} = 87\tau_{\text{vis}}$). The contours are labeled as in Fig. 9.

changes the equilibrium configuration of the star significantly, causing a redistribution of various energies. Figure 21 shows the time evolution of various energies defined in Eqs. (57)-(62). The mass of the system decreases by 1.4% due to a small amount of mass flowing out of the grid (not visible in the graph). The rotational kinetic energy T decreases slightly. The contraction of the core raises the gravitational binding energy $|W|$, as well as the adiabatic part of the internal energy M_{ic} . Viscous heating generates the thermal energy M_{ih} , which prevents the star from undergoing catastrophic collapse.

In the rapid-cooling case, star II collapses dynamically at time $t \approx 57P_{\text{rot}} \approx 17.4\tau_{\text{vis}}$. An apparent horizon appears at $t = 57.7P_{\text{rot}}$. The mass and angular momentum of the final black hole are estimated by solving Eqs. (74)–(82): $M_h \approx 0.88M$ and $J_h \approx 0.63J$ ($J_h/M_h^2 \approx 0.7$). About 10% of rest mass is left as an accretion disk.

The situations for stars III and IV are similar. The inner core contracts in a quasi-stationary manner while the outer layers expand. Each system evolves into a rigidly-rotating core surrounded by a disk-like envelope. The stars do not collapse to black holes at the end of the simulations whether or not rapid cooling is imposed. Again, we do not rule out the possibility that they might collapse to black holes when enough material accretes onto

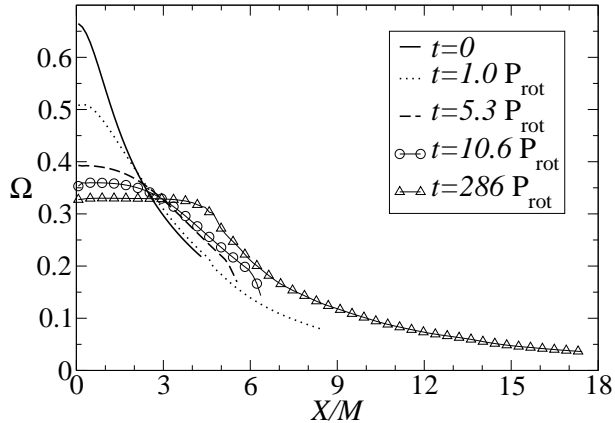


FIG. 18: Angular velocity profiles at various times in the equatorial plane for star II evolved with no cooling.

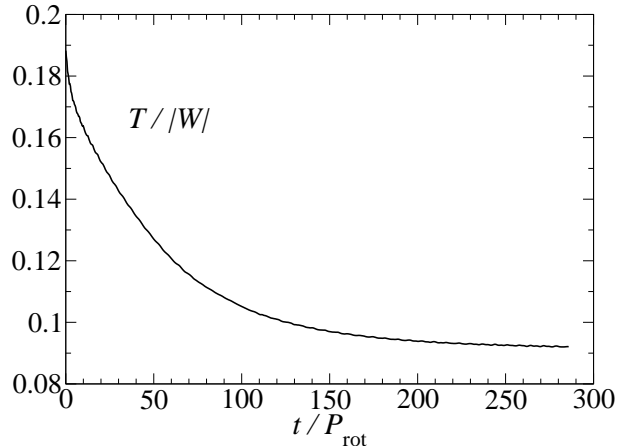


FIG. 20: Evolution of $T/|W|$ for star II evolved without cooling.

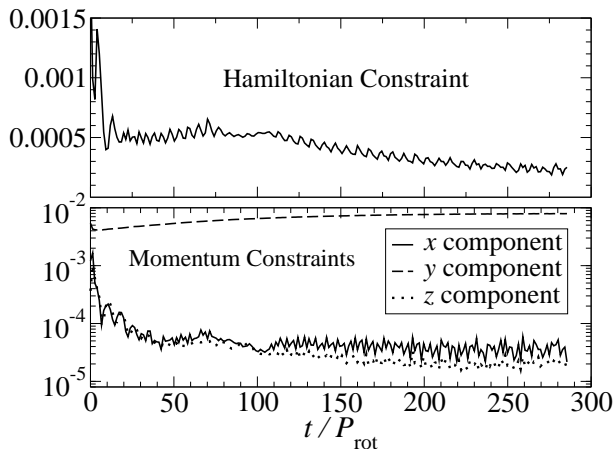


FIG. 19: L2 norms of the Hamiltonian constraint and momentum constraints for star II evolved without cooling.

the inner core.

From Table III, we see that at the end of the simulation, a large amount of angular momentum is transported to a massive disk. For stars III and IV, the rest mass of the core $M_{0,\text{core}}$ is smaller than the rest-mass limit of a supramassive star $M_{0,\text{sup}}$. For star II, $M_{0,\text{core}}$ is slightly smaller than $M_{0,\text{sup}}$ in the absence of cooling, but is slightly greater than $M_{0,\text{sup}}$ in the rapid-cooling limit. For star I, $M_{0,\text{core}} > M_{0,\text{sup}}$ in both the rapid-cooling and no-cooling cases. This suggests that the fate of a hypermassive neutron star depends on whether viscosity can create a rigidly-rotating core with $M_{0,\text{core}} > M_{0,\text{sup}}$, in which case it will collapse. Both viscous heating and the star's initial angular momentum play an important

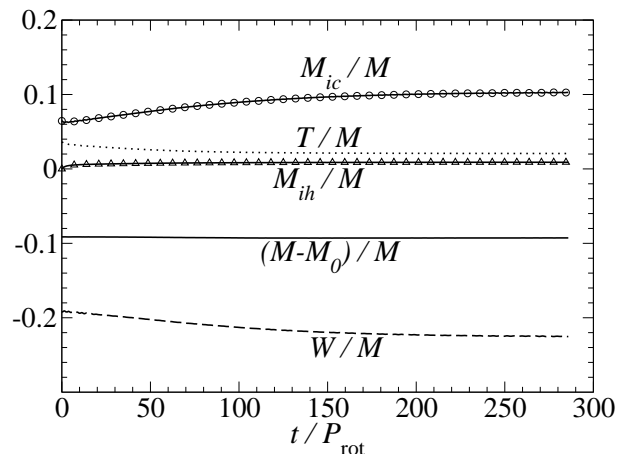


FIG. 21: Evolution of various energies for star II evolved with no cooling.

role in the final outcome. A hypermassive neutron star with higher mass and lower angular momentum is prone to collapse, whereas viscous heating tends to suppress the collapse.

Finally, we study the effect of viscosity on star V, which is non-hypermassive. As expected, the star does not collapse to a black hole, irrespective of cooling. The star eventually evolves into a rigidly-rotating core surrounded by a disk. The fact that the star does not simply become rigidly rotating without shedding mass is due to the fact that viscosity conserves M_0 and J . For a given M_0 and equation of state, there is a maximum value of angular momentum $J_{\text{max}}(M_0)$ above which a star can no

longer maintain rigid rotation without shedding mass at the equator. In the case of star V, it is apparent that $J > J_{\max}$. Hence viscosity cannot force the whole star into rigid rotation. Similar results were found in studies of viscous evolution of differentially rotating white dwarfs assuming Newtonian gravitation [40].

D. 3D tests of bar formation

The results of the axisymmetric runs described above will not be physically relevant if the models are secularly unstable to bar formation. We evolved stars I and IV in 3D to check for the formation of bars. These models were chosen because, of our five models, they have the highest values of $T/|W|$. Viscous heating can lead to expansion and, hence, a decrease in $T/|W|$. Thus, to further increase the chance of bar formation, we performed these runs in the rapid-cooling limit. We superimposed $m = 2$ perturbations on the initial data according to Eq. (72) for both stars with magnitude $\delta_b = 0.1$, so that $|Q| = 0.014$ initially. Both runs were performed in π -symmetry with a uniform grid of size $128 \times 64 \times 32$ and outer boundaries in the x - y equatorial plane at $14.3M$ for star I and $17.1M$ for star IV. To reduce computational costs, the extent of the grid in the z -direction is only half as large as in the x - and y -directions. This setup is feasible because these models are initially highly flattened due to rapid rotation and because their evolution results in an expansion which is largely horizontal. For star I, we find that $|Q|$ decreases in magnitude until the code terminates due to the collapse, when $|Q| = 0.0015$. Before the collapse, all constraints are satisfied to within 3.5% while M and J are conserved to within 3%. For star IV, $|Q|$ also decreases, reaching 0.0023 after $11.5P_{\text{rot}} = 3.3\tau_{\text{vis}}$, when the simulation is terminated. In this case, the constraints are satisfied to within 6.0% while M and J are conserved to within 1.4%. We also find that the rest density contours remain nearly axisymmetric throughout the evolutions of both stars. These results indicate that both stars are stable against secular bar formation on the viscous timescale.

V. DISCUSSION AND CONCLUSIONS

We have simulated the evolution of rapidly rotating stars in full general relativity including, for the first time, shear viscosity. Our findings indicate that the braking of differential rotation in hypermassive stars always leads to significant structural changes, and often to delayed gravitational collapse. The rest mass, angular momentum, and thermal energy all play a role in determining the final state. We performed axisymmetric numerical simulations of five models to study the influence of these parameters. In the presence of shear viscosity, the most hypermassive model which we studied (star I), collapses to a black hole whether we evolve by ignoring cooling,

or by assuming rapid cooling of the thermal energy generated by viscosity. However, the viscous transport of angular momentum to the outer layers of the star results in mass outflow and the formation of an appreciable disk. Next, we considered three hypermassive models (stars II, III, and IV) with the same rest mass M_0 , but different values of the spin parameter J/M^2 . These models have smaller M_0 than star I, and are therefore less prone to collapse. Star II, which has $J/M^2 = 0.85$, collapses when evolved in the rapid-cooling limit, leaving behind a disk. But without cooling, this model evolves to a stable, uniformly rotating core with a differentially rotating massive disk. The additional thermal pressure support provided by viscous heating prevents collapse in this case.

In contrast, stars III and IV, which have $J/M^2 = 1.0$ and 1.1, respectively, do not collapse even in the rapid-cooling limit. This is sensible because these models have a smaller rest mass than star I, but larger angular momenta than star II. Though the cores of stars III and IV contract, they are prevented by centrifugal support from reaching the necessary compaction to become dynamically unstable. In both cases, we find low-density disks surrounding uniformly rotating cores. However, our simulations do not rule out the possibility that slow accretion of the disk material could eventually drive the uniformly rotating cores to collapse. Disk formation also occurs for star V, which is differentially rotating but non-hypermassive. Since there exist stable, uniformly rotating models with the same rest mass, the braking of differential rotation in this case does not result in collapse. However, differentially rotating stars can support larger $T/|W|$ than uniformly rotating stars. In the case of star V, there does not exist a uniformly rotating star with the same (high) angular momentum and rest mass, so that mass shedding must take place as viscosity drives the star to uniform rotation. In the final state, we find a rigidly-rotating core surrounded by a low-density, disk.

Since results obtained from our axisymmetric code are physically reliable only for models which are not subject to nonaxisymmetric instabilities, we evolved stars I and IV in 3D to check for such instabilities. Previous studies in Newtonian gravity have found that the secular, viscosity-driven bar instability in uniformly rotating stars should set in when $T/|W| \gtrsim 0.14$ [1, 2]. When general relativity is taken into account, the threshold value can be somewhat higher [3]. Thus, of all of our models, stars I and IV have the best chances of developing bars since they have the highest $T/|W|$. We introduced an initial bar-shaped perturbation and ran these cases in the rapid-cooling limit. We found that, in both cases, the small initial perturbation decays and no bar is formed. This is somewhat surprising since $T/|W|$ is well above 0.14 in both of these cases. We plan to address this issue in a future report.

For the evolution of each of our five models, we find that a massive disk or torus forms in the final state. The disk typically carries $\sim 20\%$ of the rest mass of the initial configuration. Viscosity transports angular momentum

from the interior of the star to the more slowly rotating exterior. The exterior regions then expand to accommodate the additional centrifugal force, forming a low-density disk. The inner core becomes rigidly rotating and, in some cases, undergoes gravitational collapse. The disk, however, remains differentially rotating since viscosity acts much more slowly in low-density regions. For cases in which black holes are formed, the mass of the disk may be estimated by integrating the rest-mass density for those fluid elements which have specific angular momentum j greater than the value at the ISCO, j_{ISCO} [see Eq. (78)]. The estimates obtained in this way agree reasonably well with the results of our numerical simulations. Particularly good agreement was found for the case of star I with no cooling, for which we were able to extend the evolution some $55M$ beyond the first appearance of an apparent horizon. The rest mass and angular momentum of the disk surrounding the rotating black hole could then be calculated directly and agreed well with the estimates. We expect that excision techniques will continue to be crucial in establishing the final fate of systems involving matter surrounding black holes.

In a recent paper, Shibata [21] numerically simulated collapses of marginally stable, supramassive stars. These supramassive models were constructed using polytropic equations of state with $2/3 < n < 2$ and rotate at the mass-shedding limit with $0.388 \leq J/M^2 \leq 0.670$. Shibata found that the collapse of these stars results in Kerr black holes and that no more than 0.1% of the initial rest mass remains outside of the hole. This result is quite different from our finding that disks are usually present following collapse. However, the initial data for the two calculations are quite different, as well as our inclusion of viscosity. The analysis of [21] takes uniformly rotating, unstable configurations as initial data and follows their dynamical evolution. Our calculations begin with differentially rotating, stable configurations and follow both their secular (viscous) and dynamical evolution. Viscosity drives our configurations to uniform rotation. We find that massive disks usually form as by-products of the formation of uniformly rotating cores. This is due primarily to the transport of angular momentum from the inner to the outer layers. In addition, all of our models have $0.85 \leq J/M^2 \leq 1.1$. (Large angular momentum is required to generate a hypermassive neutron star in equilibrium.) Since this range is higher than that considered in [21], our models more naturally produce disks [58].

All of the phenomena observed in our simulations follow from the braking of differential rotation in strongly relativistic stars. This may be accomplished by viscosity as shown here, but magnetic fields are likely to be more important. The fate of the hypermassive remnants of binary neutron star mergers may crucially depend on these effects. The loss of differential rotation support in such a remnant may lead to delayed gravitational collapse. This collapse could in turn lead to a delayed gravitational wave burst following the quasi-periodic inspiral and merger

signal [7]. Our results indicate that if the remnant is not sufficiently hypermassive, collapse may not occur, at least not until the star cools by radiating away its thermal energy. Understanding the evolution of such merger remnants could aid the interpretation of signals observed by ground based gravitational wave detectors, such as LIGO, VIRGO, GEO, and TAMA. In addition, short-duration GRBs are thought to result from mergers of binary neutron stars or neutron star-black hole systems [22, 59]. In this scenario, the GRB may be powered by accretion from a massive torus or disk surrounding a rotating black hole. We have demonstrated that such disks are easily produced during the evolution of hypermassive neutron stars.

The braking of differential rotation may also be important in neutron stars formed in core collapse supernovae. Nascent neutron stars are probably characterized by significant differential rotation (see, e.g., [60, 61, 62, 63] and references therein). Conservation of angular momentum during the collapse is expected to result in a large value of $T/|W|$. However, uniform rotation can only support small values of $T/|W|$ without shedding mass ([38], Chap. 7). Thus, nascent neutron stars from supernovae probably rotate differentially. If the induced differential rotation is strong enough, hypermassive neutron stars can form. Their subsequent evolution and final fate then depends on the presence of viscosity or magnetic fields. Such considerations may be important for long-duration GRBs in the collapsar model [64]. In this model, the GRB is powered by accretion onto the central black hole formed through core collapse in a massive star.

Several interesting astrophysical systems undergo secular evolution in strongly gravitating environments. In this paper, we have shown that it is possible to study secular effects that occur over many dynamical timescales using hydrodynamic computations in full general relativity. We consider this an important step toward future numerical explorations of secular effects in other contexts. In particular, we plan to incorporate MHD into our evolution code, as magnetic braking probably acts more quickly than viscosity to destroy differential rotation in many systems, like neutron stars or supermassive stars [65]. Our results have also raised the following interesting question: Under what circumstances are differentially rotating, compressible neutron stars with high $T/|W|$ unstable to nonaxisymmetric modes? We plan to address this issue in a future report.

Acknowledgments

The calculations for this paper were performed at the National Center for Supercomputing Applications at the University of Illinois at Urbana-Champaign (UIUC). This paper was supported in part by NSF Grants PHY-0090310 and PHY-0205155 and NASA Grant NAG 5-10781 at UIUC.

APPENDIX A: VISCOUS HEATING AND RADIATIVE COOLING

In this appendix, we describe the thermal properties of our configurations. The dissipation of rotational energy by viscosity heats the stars, but they may be cooled by radiation (e.g. neutrino radiation). The presence of radiation contributes a term $R^{\alpha\beta}$ to the stress tensor: $T_{\text{total}}^{\mu\nu} = T^{\mu\nu} + R^{\mu\nu}$, with $T^{\mu\nu}$ given by Eq. (7). This modifies the equations of motion (13) to

$$T^{\mu\nu}{}_{;\nu} = -R^{\mu\nu}{}_{;\nu} = G^\mu, \quad (\text{A1})$$

where G^μ is the 4-force density due to radiation (see [66]). The specific entropy s of a fluid element with temperature T and number density $n = \rho_0/m$ changes when there is heating and cooling according to

$$nT \frac{ds}{d\tau} = \Gamma_{\text{heat}} - \Lambda = \Gamma_{\text{vis}} + \Gamma_{\text{rad}} - \Lambda_{\text{rad}}, \quad (\text{A2})$$

where τ is the proper time along the element's worldline. Here, we have separated the contributions from viscosity and radiation to the heating rate. The quantity Γ_{vis} is the viscous heating rate per unit volume, which comes from the $\sigma_{\alpha\beta}\sigma^{\alpha\beta}$ term in Eq. (16). In terms of the thermal energy density U_{therm} and viscous timescale τ_{vis} , Γ_{vis} is roughly

$$\Gamma_{\text{vis}} \simeq U_{\text{therm}}/\tau_{\text{vis}}. \quad (\text{A3})$$

In general, a fluid can be heated and cooled by the presence of a radiation field. The energy equation becomes

$$u_\mu T^{\mu\nu}{}_{;\nu} = u_\nu G^\nu = -G^{\hat{0}}, \quad (\text{A4})$$

where the last equality arises from evaluating $u_\mu G^\mu$ in the comoving orthonormal frame of the fluid, where $u^{\hat{\mu}} = (1, 0, 0, 0)$. Then

$$G^{\hat{0}} = \Gamma_{\text{rad}} - \Lambda_{\text{rad}} = \iint d\nu d\Omega (\kappa_\nu I_\nu - \eta_\nu), \quad (\text{A5})$$

where the integral is evaluated in the comoving frame and κ_ν , I_ν , and η_ν are the opacity, intensity, and emissivity at frequency ν [66]. For applications of interest here, radiation mediates *net* cooling of the viscous-heated fluid. Hence, we can set $\Gamma_{\text{rad}} = 0$ for simplicity.

The first law of thermodynamics

$$d(e/n) = -Pd(1/n) + Tds, \quad e \equiv \rho_0(1 + \epsilon) \quad (\text{A6})$$

and Eq. (9) give

$$\begin{aligned} nTds &= n^\Gamma d \left(\frac{Pn^{-\Gamma}}{\Gamma - 1} \right) \\ &= \frac{n^\Gamma}{\Gamma - 1} d\kappa. \end{aligned} \quad (\text{A7})$$

Here we define the entropy parameter κ by $P \equiv \kappa n^\Gamma$, where, in general, $\kappa = \kappa(s)$. The form of Λ_{rad} will depend on the details of the neutron star's microphysics, but it must have the property that $\Lambda_{\text{rad}} = 0$ when $\kappa(s) = \kappa_0 = \kappa(s=0)$, where κ_0 is the value of κ for the unheated fluid (i.e. no emission from a zero-entropy fluid). Accordingly, we replace Eq. (A5) for Λ_{rad} by the following illustrative form

$$\Lambda_{\text{rad}} = \xi n [\kappa(s) - \kappa_0] / \tau_{\text{cool}}, \quad (\text{A8})$$

where ξ is a constant and τ_{cool} is the radiation timescale. Combining equations (A2)-(A8), we find

$$\frac{d\kappa}{d\tau} = \frac{\Gamma - 1}{n^\Gamma} \left\{ \frac{U_{\text{therm}}}{\tau_{\text{vis}}} - \frac{\xi n [\kappa(s) - \kappa_0]}{\tau_{\text{cool}}} \right\}. \quad (\text{A9})$$

In the limit $\tau_{\text{cool}} \gg \tau_{\text{vis}}$, radiative cooling is unimportant and κ increases due to viscous heating. We refer to this regime as the *no-cooling* limit. If $\tau_{\text{cool}} \ll \tau_{\text{vis}}$, then the first term on the right hand side of Eq. (A9) may be dropped in relation to the second, giving

$$\frac{d}{d\tau} (\kappa - \kappa_0) = -\frac{\xi(\Gamma - 1)}{n^{\Gamma-1}} \frac{(\kappa - \kappa_0)}{\tau_{\text{cool}}}. \quad (\text{A10})$$

Thus, κ is exponentially driven to κ_0 . We refer to this regime as the *rapid-cooling* limit, whereby the thermal energy generated by viscosity is radiated immediately and does not heat the gas. In effect, $\Lambda_{\text{rad}} = \Gamma_{\text{vis}}$ in this limit. In practice we implement this limit by omitting the $\sigma_{\mu\nu}\sigma^{\mu\nu}$ in Eq. (16). Though we consider only these two limits in our analysis, we expect that, in reality, heating will dominate in some regimes and cooling in others. We treat both limiting cases in our simulations.

-
- [1] S. Chandrasekhar, *Ellipsoidal Figures of Equilibrium* (New Haven: Yale Univ. Press, 1969).
 [2] W. H. Press, and S. A. Teukolsky, *Astrophys. J.*, **181**, 513 (1973); D. Lai, F. A. Rasio, and S. L. Shapiro, *Astrophys. J. Supp.*, **88**, 205 (1993); D. Skinner, and L. Lindblom, *Astrophys. J.*, **461**, 920 (1996).
 [3] S. Bonazzola, J. Friebe, and E. Gourgoulhon, *Astro-*

- phys. J.*, **460**, 379 (1996); S. L. Shapiro, and S. Zane, *Astrophys. J. Supp.*, **117**, 531 (1998); T. D. Girolamo, and M. Vietri, *Astrophys. J.*, **581**, 519 (2002); D. Gondok-Rosinska, and E. Gourgoulhon, *Phys. Rev. D*, **66**, 044021 (2002).
 [4] L. Lindblom, B. J. Owen, and S. M. Morsink, *Phys. Rev. Lett.*, **80**, 4843 (1998).

- [5] P.B. Jones, Phys. Rev. Lett., **86**, 1384 (2001); P.B. Jones, Phys. Rev. D, **64**, 084003 (2001); L. Lindblom, and B.J. Owen, Phys. Rev. D, **65**, 063006 (2002).
- [6] L. Lindblom, and S. Detweiler, Astrophys. J., **211**, 565 (1977); L. Lindblom, and W. Hiscock, Astrophys. J., **267**, 384 (1983).
- [7] T. W. Baumgarte, S. L. Shapiro, and M. Shibata, Astrophys. J. **528**, L29 (2000).
- [8] N. D. Lyford, T. W. Baumgarte, and S. L. Shapiro, Astrophys. J., **583**, 410 (2003).
- [9] F. A. Rasio and S. L. Shapiro, Astrophys. J. **401**, 226 (1992); **432**, 242 (1994); Class. Quant. Grav. **16** R1 (1999).
- [10] M. Shibata and K. Uryū, Phys. Rev. D **61**, 064001 (2000).
- [11] M. Shibata, K. Taniguchi, and K. Uryū, Phys. Rev. D., in press (gr-qc/0310030).
- [12] S. L. Shapiro, Astrophys. J. **544**, 397 (2000).
- [13] J. N. Cook, S. L. Shapiro, and B. C. Stephens, Astrophys. J., in press (also astro-ph/0310304).
- [14] Y. T. Liu and S. L. Shapiro, Phys. Rev. D., **69**, 044009 (2004).
- [15] H.C. Spruit, Astro. & Astrophys., **349**, 189 (1999).
- [16] S.A. Balbus and J.F. Hawley, Rev. Mod. Phys., **70**, 1 (1998).
- [17] A similar approach has been suggested in [18] to simulate r -mode evolution and has been successfully applied in [19].
- [18] L. Rezzolla, M. Shibata, H. Asuda, T. W. Baumgarte, and S. L. Shapiro, Astrophys. J., **525**, 935 (1999).
- [19] L. Lindblom, J. E. Tohline, and M. Vallisneri, Phys. Rev. Lett. **86** 1152, (2001); P. Gressman, L.M. Lin, W.M. Suen, N. Stergioulas, and J.L. Friedman, Phys. Rev. D., **66**, 041303 (2002).
- [20] M. Shibata, T. W. Baumgarte, and S. L. Shapiro, Phys. Rev. D **61** 044012 (2000).
- [21] M. Shibata, Astrophys. J. **595**, 992 (2003).
- [22] M. Ruffert and H.-Th. Janka, Astron. Astrophys. **344**, 573 (1999); S. Rosswog, E. Ramirez-Ruiz, M. B. Davies, submitted to Mon. Not. Roy. Astro. Soc. (astro-ph/0306418).
- [23] T. W. Baumgarte and S. L. Shapiro, Phys. Rev. D, **59**, 024007 (1999); M. Shibata and T. Nakamura, Phys. Rev. D **52**, 5428 (1995)
- [24] M. D. Duez, P. Marronetti, S. L. Shapiro, and T. W. Baumgarte, Phys. Rev. D, **67**, 024004 (2003). (Paper I)
- [25] M. D. Duez, S. L. Shapiro, and H.-J. Yo, Phy. Rev. D, in press (gr-qc/0401076).
- [26] C. W. Misner, K. S. Thorne, and J. A. Wheeler, *Gravitation* (Freeman, New York, 1973), p. 566.
- [27] M. Alcubierre, S. Brandt, B. Brügmann, D. Holz, E. Seidel, R. Takahashi, and J. Thornburg, Int. J. Mod. Phys. **D10**, 273 (2001).
- [28] M. Shibata, Prog. Theor. Phys. **104**, 325 (2000).
- [29] N. Stergioulas, and J. L. Friedman, Astrophys. J., **492**, 301 (1998); S. Morsink, N. Stergioulas, and S. Blattning, Astrophys. J., **510**, 854 (1999); S. Yoshida, L. Rezzolla, S. Karino, and Y. Eriguchi, Astrophys. J., **568**, L41 (2002).
- [30] J. L. Friedman, and B. F. Schutz, Astrophys. J., **199**, L157 (1975); J. L. Friedman, and B. F. Schutz, Astrophys. J., **221**, L99 (1978).
- [31] E. Flowers and N. Itoh, Astrophys. J. **230**, 847 (1979).
- [32] C. Cutler and L. Lindblom, Astrophys. J. **314**, 234 (1987).
- [33] J. M. C. Chen, J. W. Clark, R. D. Davé, and V. V. Khodel, Nucl. Phys. A **555**, 59 (1993).
- [34] M. Hoffberg, A. E. Glassgold, R. W. Richardson, and M. Ruderman, Phys. Rev. Lett. **24**, 175 (1970).
- [35] E. Flowers and N. Itoh, Astrophys. J. **206**, 218 (1976).
- [36] G. Mendell, Mon. Not. R. Astron. Soc. **296**, 903 (1998).
- [37] M. A. Alpar, S. A. Langer, and J. A. Sauls, Astrophys. J. **282**, 533 (1984).
- [38] S. L. Shapiro and S. A. Teukolsky, *Black Holes, White Dwarfs, and Neutron Stars* (Wiley, New York, 1983).
- [39] C. J. Pethick, Rev. Mod. Phys. **64**, 1133 (1992).
- [40] R. H. Durisen, Astrophys. J., **183**, 205 (1973); R. H. Durisen, Astrophys. J., **183**, 215 (1973); R. H. Durisen, Astrophys. J., **195**, 483 (1975).
- [41] L. D. Landau and E. M. Lifshitz, Fluid Mechanics (Butterworth-Heinemann, 1987)
- [42] T. W. Baumgarte and S. L. Shapiro, Astrophys. J. **504**, 431 (1998).
- [43] M. Shibata, Phys. Rev. D **67**, 024033 (2003).
- [44] H. O. Kreiss and J. Olinger, *Methods for the Approximate Solution of Time Dependent Problems*, GARP Publication Series No. 10 (World Meteorological Organization, Geneva, 1973); A. M. Abrahams, G. B. Cook, S. L. Shapiro, and S. A. Teukolsky, Phys. Rev. D **49**, 5153 (1994); M. W. Choptuik, E. W. Hirschmann, S. L. Liebling, and F. Pretorius, Class. Quant. Grav. **20**, 1857 (2003).
- [45] N. Ó. Murchadha and J. W. York Jr., Phys. Rev. D **10**, 2345 (1974); J. M. Bowen and J. W. York, Jr., Phys. Rev. D **21**, 2047 (1980).
- [46] R. M. Wald, *General Relativity* (Univ. of Chicago, Chicago, 1984), p. 297.
- [47] G. B. Cook, S. L. Shapiro, and S. A. Teukolsky, Astrophys. J. **398**, 203 (1992).
- [48] H. J. Yo, T. W. Baumgarte, and S. L. Shapiro, Phys. Rev. D **64**, 124011 (2001).
- [49] In Paper I, star A was labeled “C” and star B was labeled “D”.
- [50] Y. Eriguchi and E. Müller, Astro. & Astrophys., **146**, 260 (1985).
- [51] J. L. Friedman, J. R. Ipser, and R. D. Sorkin, Astrophys. J. **325**, 722 (1988).
- [52] M. Shibata, T. W. Baumgarte, and S. L. Shapiro, Astrophys. J. **542**, 453 (2002).
- [53] M. Shibata, Phys. Rev. D **60**, 104052 (1999).
- [54] M. Saijo, T. W. Baumgarte, and S. L. Shapiro, Astrophys. J. **595**, 352 (2003).
- [55] L. Villain, J. A. Pons, P. Cerda-Duran, E. Gourgoulhon, astro-ph/0310875 (2003).
- [56] What appears to be a drift in M_h due to numerical error becomes visible towards the end of the simulation. This makes the extrapolated value of M_h less reliable than the values of $M_{0,disk}$ and J_{disk} .
- [57] S. L. Shapiro, and M. Shibata, Astrophys. J. **577**, 904 (2002).
- [58] Disks *can* form from the collapse of uniformly rotating polytropes near the mass-shedding limit, provided $n \approx 3$ [see M. Shibata and S. L. Shapiro, Astrophys. J. **577**, 904 (2002)].
- [59] R. Narayan, T. Piran, and P. Kumar, Astrophys. J. **557**, 949 (2001).
- [60] T. Zwerger and E. Müller, Astron. Astrophys. **320**, 209 (1997).

- [61] M. Rampp, E. Müller, and M. Ruffert, *Astron. Astrophys.* **332**, 969 (1998).
- [62] Y. T. Liu and L. Lindblom, *Mon. Not. R. Astron. Soc.* **342**, 1063 (2001).
- [63] Y. T. Liu, *Phys. Rev. D* **65**, 124003 (2002).
- [64] A. MacFadyen and S. E. Woosley, *Astrophys. J.* **524**, 262 (1999).
- [65] G. S. Bisnovatyi-Kogan, Ya. B. Zel'dovich, and I. D. Novikov, *Sov. Astron.* **11**, 419 (1967); T. W. Baumgarte and S. L. Shapiro, *Astrophys. J.* **526**, 941 (1999); K. C. B. New and S. L. Shapiro, *Astrophys. J.* **548**, 439 (2001).
- [66] D. Mihalas and B. Weibel-Mihalas, *Foundations of Radiation Hydrodynamics* (Dover, Mineola, 1999); S. L. Shapiro, *Astrophys. J.* **472**, 308 (1996).